ISSN 2718-322X (Online)

Engineering Power

BULLETIN OF THE CROATIAN ACADEMY OF ENGINEERING Vol. 21(1) 2026

Euro-CASE CAETS

EDITOR-IN-CHIEF'S WORD

Dear readers,

It is a privilege to introduce this issue of Engineering Power, a publication that reflects the Croatian Academy of Engineering's commitment to knowledge, responsibility, and progress.

The journal serves as an important meeting point for research, professional experience, and new ideas. It gives visibility to work that can influence technological advancement, public policy, economic development, and the quality of life. Through this role, Engineering Power also strengthens the presence of engineering in wider social debate.

The Croatian Academy of Engineering brings together leading experts from different fields and encourages them to contribute to matters of national and international importance. Its task is not only to recognise achievement, but also to support cooperation, sound professional judgement, and the responsible application of technology.

The contributions in this issue illustrate how engineering can respond to complex contemporary needs through creativity, precision, and collaboration across disciplines. I trust that they will encourage further thought and provide useful perspectives to our readers.

Editor-in-Chief
Vedran Mornar, President of the Croatian Academy of Engineering

EDITOR'S WORD

Dear readers,

It is my great pleasure to present the new issue of the Engineering Power journal, edited by Prof. Neven Duić, PhD. The papers in this issue are related to the SDEWES conference, held under the auspices of the Croatian Academy of Engineering. In this issue, you will have the opportunity to read about the use of vortex generators on the blades of a vertical-axis current turbine, a smart charging strategy for electric vehicles used in Italy, and the comprehensive remediation of polluted waters using a compact composite layered material. I hope you enjoy reading this issue.

Editor
Bruno Zelić, Vice-President of the Croatian Academy of Engineering

FOREWORD

With a broad vision of integrating various systems for long-term sustainability, the international conference series on the sustainable development of energy, water, and environmental frameworks was launched at the beginning of the 21st century. Now in its third decade since the first gathering in Dubrovnik, Croatia, which set the foundation for the series in 2002, the need for this integrated perspective has never been more pressing. Utilizing surplus from one system as a resource for another at the right moment is one of the most crucial challenges in preserving the Earth's essential support systems. Enhancing the efficiency of interconnected systems, spanning electricity, heating, cooling, transportation, water management, waste treatment, industrial operations, construction, forestry, and agriculture, serves as a key strategy for reducing environmental impact while allowing development to progress. This holistic approach to sustainability offers significant opportunities for accelerating efforts toward reducing carbon emissions and tackling climate change.

The field of engineering is well-positioned to address sustainability challenges, but it must move beyond rigid disciplinary boundaries and embrace the need for equipping future professionals with diverse competencies. The technical solutions required to lower environmental impact while retaining the conveniences of modern life are inherently interdisciplinary, drawing from electrical, mechanical, information, civil, chemical, food-related, and other engineering disciplines, as well as architecture, economics, agriculture, and forestry.

This edition presents three forward-looking innovations in technology and methodology for assessing sustainability that could contribute to a more environmentally responsible way of life.

Rahuna et al. show, through CFD simulations, that rectangular vortex generators on NACA 0021 turbine blades delay stall, reduce drag, and improve lift-to-drag performance [1]. The optimal design increased the predicted power output of a vertical-axis marine current turbine by about 7.5%, demonstrating a simple method for improving turbine efficiency.

Aleotti et al. propose a real-time, forecast-free charging strategy for electric vehicles in Italian Renewable Energy Communities [2]. By coordinating charging with local photovoltaic generation, the approach increased shared energy by about 47% and community incentive revenues by about 50%, while maintaining normal vehicle availability.

The third paper presents a clay-birnessite/buserite composite capable of simultaneously removing heavy metals and organic pollutants from water. The study highlights its high adsorption capacity, low cost, and potential as a scalable and sustainable solution for advanced water treatment [3].

References

[1] D. Rahuna, I. K. A. P. Utama, Erwandi and D. Satrio, "An investigation into the use of vortex generators on the blade of vertical axis current," Engineering Power, vol. 21, no. 1, pp. 2-14, 2026.

[2] F. Aleotti, A. Rollo, P. Marcolin, V. Angelucci, D. Cilio and M. Zulianello, "A new smart charging strategy for electric vehicles in energy communities: An Italian case study," Engineering Power, vol. 21, no. 1, pp. 14-29, 2026.

[3] K. Xhaxhiu, A. Berisha, N. Isak, B. Baraj and B. Seiti, "Toward a comprehensive remediation of polluted waters using," Engeineering Power, vol. 21, no. 1, pp. 29-37, 2026.

Guest Editor
Neven Duić, University of Zagreb, Faculty of Mechanical Engineering and Naval Architecture

CONTENT

Editors' Words 1
1. An investigation into the use of vortex generators on the blade of vertical axis current turbine in correlation with delaying stall and increasing energy efficiency 2
2. A new smart charging strategy for electric vehicles in energy communities: An Italian case study 14
3. Toward a comprehensive remediation of polluted waters using a compact composite layered material 29

Daif Rahuna [1,2], I Ketut Aria Pria Utama [3,], Erwandi [2], Dendy Satrio [1]*

An investigation into the use of vortex generators on the blade of vertical axis current turbine in correlation with delaying stall and increasing energy efficiency

[1]Departement of Ocean Engineering, Institut Teknologi Sepuluh Nopember (ITS), Surabaya, Indonesia
[2]National Research and Innovation Agency (BRIN), Surabaya, Indonesia
[3]Departement of Naval Architecture, Institut Teknologi Sepuluh Nopember (ITS), Surabaya, Indonesia
*Corresponding author: kutama@its.ac.id

Original scientific paper
Received: December 15, 2025
Accepted: May 13, 2026
https://doi.org/10.65776/ep.21.1.1

Abstract

The common phenomena in vertical-axis turbines arise from the continuously changing angle of attack (AoA), which results in; flow separation, dynamic stall, unsteady hydrodynamics, complex wake and vortex structures, and Cyclic structural loading. Devices such as vortex generators (VGs) are used to mitigate flow separation and dynamic stall, thereby significantly improving turbine performance. Numerical simulations investigate the effect of VG addition on turbine performance in general, specifically the NACA 0021 blades in the H-type Darrieus turbine. The single-blade model was equipped with rectangular VGs of specific dimensions, arranged in a single row and contra rotating. Computational Fluid Dynamics (CFD) simulation using ANSYS-FLUENT was employed as the numerical approach to compare the performance of an NACA 0021 blade with and without rectangular VGs. The VGs were placed at chordwise positions of 20%c, 25%C, and 30%c. The simulation results show that the most effective VG placement is at 25%c, where the drag coefficient is reduced by up to 38.0% at an AoA of 15°, and by 17.3% at AoA = 20°, compared to the clean airfoil without VGs. This study shows that the addition of VGs reduces drag and enhances turbine performance. The reduction in drag influences the flow separation behavior, thereby delaying stall.

***Keywords**: Vortex Generator, Drag Reduction, Stall Delay, airfoil NACA 0021, Vertical Axis Ocean Current Turbine (VACT)*

1. Introduction

Flow control approaches can be utilized to prevent boundary layer (BL) separation and stalling. Vortex generators (VGs) were originally proposed by Taylor in 1947 [1], to increase lift and decrease drag by delaying stall at an aircraft's wing, in aviation [2]. When VG is on the upper surface of the wing, it helps maintain airflow attachment to the wing at high angles of attack, reducing stall speed and/or making the control surfaces more effective. The Boeing 737 utilizes VG devices not only on the wings but also on the horizontal stabilizer and the forward fuselage. The addition of VGs serves to stabilize airflow over the vertical and horizontal stabilizers, help control airflow at high speeds, and reduce hydrodynamic noise that could disturb the pilot [3].

In the energy sector, VGs are the best choice to improve the performance of horizontal axis wind turbines (HAWTs), due to their good enhancement effect, low cost, and easy application [4]. VGs transfer momentum from the outside free-stream flow to the wall area, then increase the near-wall momentum, when the flow is separated from the blade surface in a smooth blade case [5]. The condition known as dynamic stall is a dynamic and unstable phenomenon. In addition, VGs can minimize vibration, noise, and fatigue stresses caused by stalls on the blades, to improve performance and energy production, thus attracting much research interest [6][7].

In general, vertical axis current turbines (VACTs) have disadvantages, especially in low turbine performance efficiency, poor self-starting, cavitation, and vibration [8] [9]. However, VACTs have advantages including, accepting flow from all directions, easy maintenance, low cost and simple construction. Therefore, this has driven researchers to develop VACT. Many studies have developed VACT, aiming to improve turbine performance in recent decades.

Extensive research has been conducted to improve the self-starting capability of VACTs, including modifications to turbine geometry and flow control approaches. The geometric modifications involve variable pitch control [10][11], inclined blades [12], changes in blade angle [13], the addition of auxiliary rotors [14], the use of winglets [15][16][17], and helical blades [18]. Meanwhile, augmentation devices are used to alter the fluid flow behaviour around VACTs, such as flow disruption [19] [20], flow deflectors [21], tubercles [22][23], and VGs, which are the focus of this study.

Several recent VG studies have been developed to gain more details on the flow mechanism and the best VG shape design methodology to produce optimal VG performance on aerofoil types. The best VG design is often based on vortex peaks, vorticity trajectories, dimensions, and steady flow velocity. Dimensions, placement location and configuration play an important role in accelerating vortex formation, thereby improving aerofoil performance [24][25]. These studies suggest that no single VG model has proven superior to others in representing the impact of VGs on flow using body forces [5][26]. Mueller-Vahl et al. observed that a small VG distance not only resulted in a stall delay of up to 12.5° from the stall AoA, and a 31% increase in the maximum lift coefficient ($C_{l,max}$), but also reduced the drag coefficient. Reducing the distance causes increased interaction of the surrounding vortices so that the vortices move further from the airfoil surface [27]. A study on the DU97-W-300 airfoil with added VGs showed that the chordwise position of the VGs and the blade height were the most important factors for airfoil performance, but blade length, pitch angle, blade shape, and stacking density proved to be secondary factors [28]. In another study, the influence of rectangular VGs arranged in a dual-row configuration on the flow around the NREL S809 airfoil was investigated through numerical simulation. The findings revealed that the second row of VGs contributed to a greater suppression of flow separation, leading to a $C_{l,max}$. increase of 0.27 compared to the single-row configuration positioned near the leading edge [29]. The study conducted by Binbin Wei et al. investigated the use of VGs as a passive flow control method to reduce dynamic stall on wind turbine and helicopter rotor airfoils. Using a NACA 0012 airfoil and wind tunnel experiments, the study showed that VG installation could delay flow separation, reduce dynamic stall vortices, and improve aerodynamic stability at high angles of attack. The research also found that the position and configuration of the VG greatly affect its effectiveness in improving aerodynamic performance [30].

The purpose of this study is to explore the stall delay, lift force and drag force to maximize turbine performance by obtaining the highest lift and lowest drag and to assess the flow pattern affected by the addition of VG. The profile used as a benchmark is NACA 0021, a 21% thick airfoil with a chord of 0.14 m and a span of 0.28 m, at a Reynolds number of 1.917×10^5. Furthermore, we add VG to the surface of both rectangular profiles, adjusting their placement and dimensions accordingly. The approach uses numerical simulation to analyze the effect of VG on the NACA 0021 airfoil of VACT with the Reynolds-averaged Navier-Stokes (RANS), based Computational Fluid Dynamics (CFD) approach using the k-ω SST (shear stress transport) of turbulence model.

1.1 State of the art

This study differs from previous research by placing the VG below the hydrofoil profile in the CFD analysis. The investigation covers an angle of attack range from 0° to 45° in the turbine rotation direction, whereas previous studies commonly installed VGs on the upper profile. It is like the aeroplane wings concept.

The main difference of this study compared to previous ones is associated with the designation of the positive azimuthal angle (θ^+). While rotating from $\theta = 0°$, the azimuthal angle is designated as positive (θ^+), while the projected angle of attack is named as the positive angle of attack (α^+). If blade rotation is happening towards $\theta = 0°$, the azimuthal angle is named negative (θ^-), while the projected angle of attack is called the negative angle of attack (α^-). Much research has been done with profiles incorporating VG at moderate negative angles of attack, whereas there is very little data for positive angles of attack.

This arrangement is especially crucial since the turbine blade meets the incoming stream at the highest velocity relative to each other in this case. Therefore, the blade experiences the greatest hydrodynamic force that is necessary for creating rotation, which improves the efficiency of the turbine.

2. Methodology

In this paper, the numerical simulation approach used is on a single blade, where a single blade is a blade that does not cover the entire turbine, while in general, the turbine consists of several blades (more than one). The model used in the numerical simulation includes the original blade in the form of a symmetrical NACA-0021 foil without and with the addition of VGs, where the VG is rectangular with differences in placement on the foil surface. The purpose of this numerical simulation is to provide initial insight into the effects of adding VGs to the blades compared to no VGs, as well as the effects of VG shape and placement on stall delay, lift coefficient (C_l), and drag coefficient (C_d).

This section explains the flowchart that clearly and concisely outlines the step-by-step process of the research, serving as a focused framework for evaluating the effectiveness of adding VGs to improve the performance of the NACA 0021 foil used as a blade in a VACT system. The main procedural steps are illustrated in **Fig. 1**. The initial step involves defining the geometry and preparing the computational domain, which is described in detail. The next steps include mesh generation, a grid independence study, boundary condition configuration, and solver setup. The validation process involves evaluating solver settings and remeshing if the results deviate from the expected validation trends. The implementation of rectangular VGs in the simulation will proceed only once the validation criteria are met. The results section presents findings for three key parameters: C_l and C_d. It also includes contour analysis of the flow behavior around the blade, both with and without VGs. The final part of the study provides a performance prediction of VG implementation on VACT, specifically assessing the application of VGs on the NACA 0021 foil within a VACT configuration.

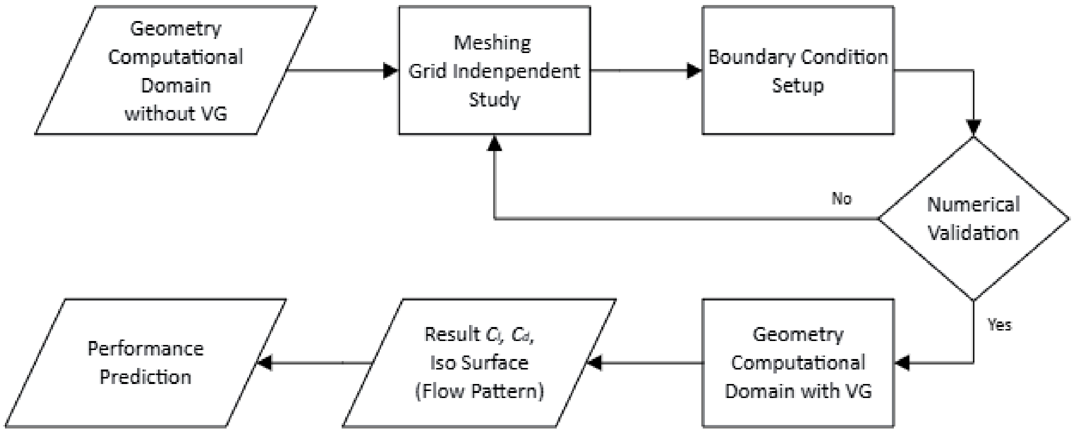

Fig. 1. CFD methodology

2.1 CFD Modelling

The computational domain was developed using ANSYS Design Modeler, with mesh generation conducted in ANSYS Meshing. To ensure fully developed flow and minimize boundary-induced effects, the domain was sized at 30*c*, consistent with best practices established in prior hydrodynamic studies [6]. The domain configuration is optimized to facilitate AoA (*α*) parameterization through the manipulation of inlet velocity components, thereby enabling the simulation of varying α without altering the hydrofoil's geometric orientation or creating multiple model instances [31].

The computational domain is cylindrical with the hydrofoil located at the center of the cylinder. The diameter of the domain is 30c to ensure that the fluid flow is fully developed [32]. It is easier to implement the inlet α parameterization. By changing the inlet velocity components to simulate different *α*, there is no need to create another model with varying orientations of hydrofoil [25]. The simulations are performed in the *α* range of 0°-45° with an increment of 5°. However, it is important to note that the angle between 0°-40° is considered as the critical *α*, so the analysis is focused on the hydrofoil performance. Therefore, the increment is increased to 2° in the range to produce a smoother curve shape and capture the phenomenon in detail [25].

The domain geometry is generated using ANSYS Design Modeler. A hybrid O-topology grid is employed for the clean profile, with the domain's radius set to 15 of the chord lengths. A hybrid O-topology grid is employed for the clean profile, with the domain's radius set to 15 of the chord lengths. The boundary conditions used during the numerical simulation, which were adjusted to match the test conditions conducted by holst, 2019. The test conditions used air as the working fluid, on a Reynolds number (*Re.*) of 1.917×10^5, a velocity of inlet 20 m/s, a turbulence intensity of 1%, and a viscosity ratio of 6 [6]. Boundary conditions in the numerical simulation are adjusted to test conditions. Side boundaries were set as symmetry to replicate the extended range used in further research. Hydrofoil surface and VG were set as no-slip wall boundary conditions. The low Reynolds number indicates that the hydrofoil may have difficulty in self-starting due to the lower fluid velocity.

2.2 Geometry Modeling

This modeling strategy enhances computational efficiency while ensuring consistent boundary conditions across all cases. It further allows for a continuous sweep of *α* values, typically ranging from 0° to 180°, which is essential for accurately capturing the hydrodynamic response of the hydrofoil, particularly in the critical stall region. Such an approach is highly advantageous for evaluating unsteady flow phenomena and performance degradation due to flow separation.

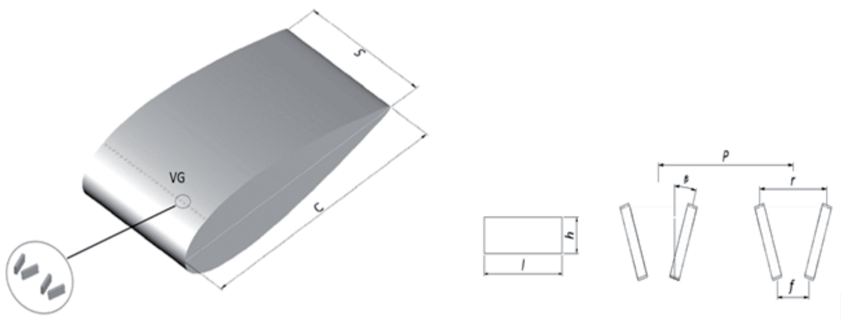

Fig. 2. VGs Schematic on the blade.

The numerical approach is done with a turbine model with and without VG addition. The shape of the VG rectangle, with VG placement location, varies between 10%-30% of chord length (c) with 5% interval, and single row contra-rotating configuration The dimensions of the VG and the shape of the VG consisting of a rectangle are shown in **Table 1**. The dimensions of VGs based on data obtained from researchers who have conducted previous research include height, *h*, (*h*/*c*), length, *p*, (*l*/*h*), angle (*β*), the distance between VG (*p*/*h*), front distance (*f*/*h*), and rear distance (*r*/*h*), as represented in **Fig. 2**.

Table 1. Turbine and VG specifications for numerical simulation.

Part	Name/parameter	Specification/value
VACT Blade	*Hydrofoil type*	NACA 0021
	Number of blade (N)	3
	Chord length (c)	0.14 m
	Span (S)	0.28 m
	Sudut pitch	0^{O}
	Angle of attack, AoA (α)	0 – 45^{o}
Vortex generator	*VG Shape*	rectangular
	Location Position	20%c, 25%c, 30%c
	Configuration	single-row, contra-rotating
	Height (h/c)	Small VG parameters, as seen in Table 2
	Length (l/h)	3
	Angle (β)	18^{o}
	Pair distance (p/h)	7
	Rear distance (r/h)	3.5
	Front distance (f/h)	1.65

In the numerical simulation of a foil with the addition of VGs, several variations are considered, including the dimensions and placement of the VGs, as shown in **Table 2**. The height of the VG changes for each difference in VG position relative to the chord length. This is because the VG height equals the boundary layer (BL) thickness at each placement location on the foil surface [33]. The relative height of VGs is typically represented by the variable h/δ, where h denotes the VG height and δ represents the boundary layer thickness. Based on their height, VGs are categorized into two types: conventional VGs ($h/\delta \geq 1$) and submerged VGs ($0.1 < h/\delta < 0.5$), also known as "micro" or "low-profile" VGs [34]. Every change in VG height always affects other VG dimensions, such as length (*l*), spacing between VG pairs (*p*), and the total number of VGs along the span for each variation of placement location (*x*/*c*).

Table 2. Main parameters of the small VGs simulated in this study.

x/c	*h (mm)*	*l (mm)*	*p (mm)*	*r (mm)*	*f (mm)*
20%	0.60	1.80	4.20	2.10	0.99
25%	0.72	2.16	5.04	2.52	1.19
30%	0.87	2.61	6.09	3.05	1.44

2.3 Validation

The grid was generated using ANSYS Meshing software. The mesh comprises three distinct regions: a structured, multi-block section in the boundary layer, an unstructured region surrounding the airfoil to maintain an approximately constant cell size, and another structured region encompassing the outer domain. For the clean profile configuration, a hybrid O-type topology is employed with a domain radius of 15c to minimize far-field boundary effects. The mesh consists of three zones: a structured multi-block region for accurate boundary layer resolution, an unstructured region around the hydrofoil for flexibility and uniform cell distribution, and an outer structured region extending to the far field to improve numerical stability and overall grid quality.The computational domain is defined as a circular region with a diameter sufficiently large to minimize boundary interference effects on the flow around the hydrofoil, as represented in **Fig.3a**. A velocity inlet boundary condition is applied at the upstream region to prescribe a uniform incoming flow. The downstream boundary is treated as an outlet, allowing the flow to exit the domain without reflection.

The lateral boundaries are defined as symmetry conditions, which imply zero normal velocity and zero normal gradients for all flow variables. This assumption reduces computational cost while maintaining physical accuracy for external hydrodynamic flow. The profile surface itself is modeled as a no-slip wall, enforcing zero velocity at the surface to capture boundary layer development.

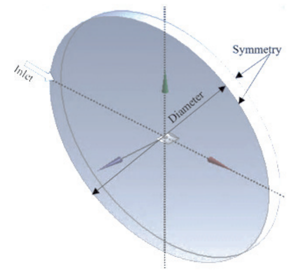

(a)

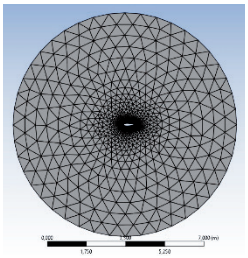

(b)

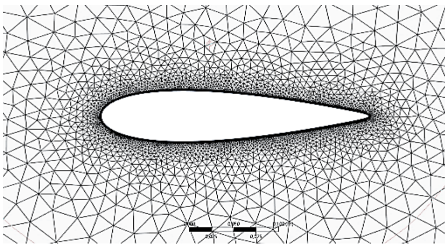

(c)

Fig. 3. Computational mesh for clean foil NACA 0021

In this study, the mesh for the original NACA 0021 foil consists of 1,467,950 elements and 407,450 nodes. The finest mesh resolution is concentrated around the foil, with a growth rate of 1.2. The overall mesh distribution within the computational domain is illustrated in **Fig. 3b**, while the refined mesh structure surrounding the foil is also depicted **Fig. 3c**. An inflation layer technique is employed along the foil surface to accurately capture the boundary layer effects, with the first layer thickness set to 0.00007636 m.

A target y^+ value of 0.85 is used to ensure adequate near-wall resolution and improve boundary layer accuracy. Keeping y^+<1 allows proper resolution of the viscous sublayer, consistent with the requirements of the *k–ω SST* turbulence model, and enables wall-resolved simulations without wall functions. This improves the prediction of shear stress and pressure distribution along the hydrofoil surface.

Table 3. Mesh Quality

Quality	Foil NACA-0021
skewness	0.2168
orthogonal quality	0.7813
aspect ratio	5.7708

To achieve this, the mesh near the wall is refined using a first inflation layer height of 1.298x10-5m, with 9 inflation layers and a growth rate of 1.2. This configuration ensures accurate capture of boundary layer development, separation, and reattachment, which is essential for evaluating the hydrodynamic performance of the hydrofoil with micro-VGs.

As summarized in **Table 3**, the generated mesh demonstrates satisfactory quality. The skewness values remain below 0.25, indicating well-shaped elements with minimal distortion. The orthogonal quality is consistently above acceptable thresholds (approaching unity), reflecting good alignment between cell faces and flow gradients. Additionally, the aspect ratio ranges between 0.5 and 0.8, suggesting balanced element proportions without excessive stretching.

Secondly, a mesh was generated for the NACA 0021 airfoil model incorporating VGs, with the height of each VG matched to the local boundary layer thickness, as shown **Fig. 4**. This thickness varies along the chordwise position (*x/c*), being thinner near the leading edge and gradually increasing toward the trailing edge, as detailed in **Table 1**. To ensure consistency, the same meshing strategy applied to the original airfoil was also used for the airfoil equipped with VGs.

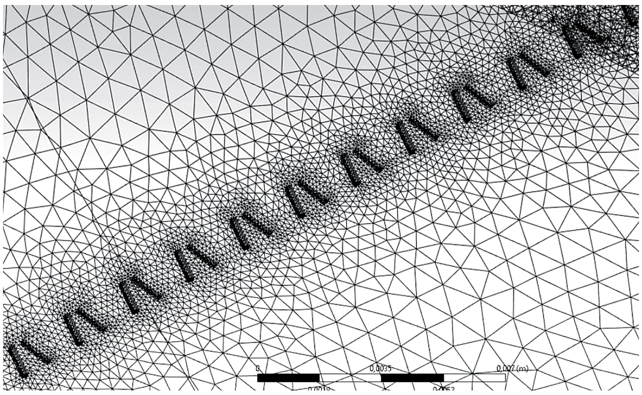

Fig. 4. Mesh generation for the foil with integrated VGs

A mesh independence study was carried out on the hydrofoil model without VG at an α of 10°. The resulting C_l and C_d from the simulation were validated against the experimental data of [6]. A grid independence test was performed using the coupled second-order upwind method to evaluate the grid independence (GI) values for C_l and C_d across varying element counts: The 365,782-element mesh is now explicitly described in the grid independence section as a preliminary mesh sensitivity check. This mesh level was initially employed to obtain a first-order assessment of solution behavior and to identify a suitable range for subsequent systematic refinement. The formal convergence study, therefore, focuses on the three progressively refined meshes—coarse (733,522 elements), medium (1,467,736 elements), and fine (2,935,503 elements), as these satisfy the requirements for consistent refinement ratio and reliable estimation of numerical uncertainty. The findings of this study elucidate the influence of element count variations on the measured values of C_l and C_d. As shown in **Table 4**, The grid independence test (GIT) conducted between the medium and fine grids yielded results of 0.019 for C_d and 0.043 for C_l.

Table 4. Verification outcomes were obtained through the application of the GI method.

Elements Number	C_d	*GI*	C_l	*GI*
365,782	0.0356408	-	0.5978161	-
733,522	0.0351602	0.032	0.6026012	0.022
1,467,736	0.0354005	0.019	0.6118848	0.043
2,935,503	0.0356692	0.060	0.6145331	0.013

The order of convergence (p) estimates how fast the numerical solution improves with grid refinement. It is computed from solutions at successive grid levels and indicates how effectively discretization error is reduced. A p value close to the method's formal accuracy shows consistent convergence, while deviations may indicate nonlinear effects or remaining numerical errors.

$$p = \frac{\ln\left|\frac{\varepsilon_{32}}{\varepsilon_{21}}\right|}{\ln(r)} \quad (1)$$

Richardson extrapolation is used to estimate the solution on an infinitely fine grid:

$$\phi_{ext} = \phi_1 + \frac{\phi_1 - \phi_2}{r^p - 1} \quad (2)$$

The GCI is calculated using the difference between solutions on refined grids, the grid refinement ratio, and the estimated order of convergence. A safety factor (Fs) is applied to provide a conservative estimate of numerical uncertainty, which is expressed as a percentage and used to assess the sensitivity of the solution to grid resolution. Fs = 1.25 is the safety factor recommended by Roache. A small GCI value indicates weak dependence of the numerical solution on grid resolution, whereas a large GCI value reflects significant sensitivity to grid refinement and non-negligible discretization errors. Formula of the GCI:

For the medium $_2$ - coarse $_1$ grid pair:

$$GCI_{21} = F_s \frac{|\phi_1 - \phi_2|}{|\phi_1|(r^p - 1)} \times 100\% \quad (3)$$

For the fine $_3$ - medium $_2$ grid pair:

$$GCI_{32} = F_s \frac{|\phi_2 - \phi_3|}{|\phi_2|(r^p - 1)} \times 100\% \quad (4)$$

Table 5. Verification outcomes were obtained through the application of the GCI method.

Elements Number	C_d	*GCI*	C_l	*GCI*
365,782*	0.03564		0.59781	
733,522	0.03516	0.013	0.60260	0.011
1,467,736	0.03540	0.009	0.61188	0.011
2,935,503	0.03566		0.61453	

** preliminary mesh sensitivity check*

Verification of the asymptotic range confirms that the solution converges consistently with grid refinement. The GCI and refinement ratio indicate the solution lies within this range, so the associated numerical uncertainty is considered valid.

$$\frac{GCI_{32}}{GCI_{21}} \approx r^p \quad (5)$$

In addition to the GI, it is also essential to assess the error ratio between two different grid resolutions, as the Grid Convergence Index (GCI) method serves as a valuable tool for understanding how errors decrease with increasing grid resolution. As shown in **Table 5**, In this verification process, numerical uncertainty is quantified using GCI method, which is based on the Generalized Richardson Extrapolation [35].

3. Result and Discussion

3.1 Lift and Drag Coefficients

The numerical simulation results were compared with experimental data using scale-resolving methods. **Fig. 5** illustrates the relationship between the lift coefficient and the variation of angle of attack (AoA), ranging from 0° to 45°, with 5° intervals. The numerical simulations were conducted for a NACA 0021 airfoil equipped with rectangular VGs, arranged in a single row at various chordwise positions (20%c, 25%c, and 30%c). The height of each VG (h) was matched to the local boundary layer thickness (δ) at each corresponding placement position. The simulation results indicate that the addition of VGs leads to an increase in lift coefficient compared to the baseline configuration without VGs, particularly at α = 15°. The most significant lift enhancement occurred at the 30%c position, where the peak lift coefficient reached 6.7%, followed by the 20%c position with a peak lift coefficient of 5.7%, and the 25%c position with 2.0%, all relative to the airfoil without VGs. At an angle of attack of 20°, the greatest increase in lift coefficient 7.4% was achieved with the VGs positioned at 25% chord. Positioning them at 30%c yielded a 5.4% increase in lift coefficient, while placement at 20%c produced a 3.7% increase.

The implementation of VGs on the airfoil led to a considerable reduction in the drag coefficient. The most significant reduction was recorded at the 25%c location, reaching 38.0%, followed by reductions at the 30%c and 20%c positions, which achieved 37.4% and 27.3%, respectively, in comparison to the baseline configuration without VGs, as shown in **Fig. 6**. At $\alpha = 20°$, the highest drag reduction was again recorded with the VG positioned at 25%c, achieving a 17.3% decrease in drag coefficient. This was followed by reductions of 10.3% and 8.3% for VG placements at 20% and 30% chord, respectively. The simulation outcomes demonstrate that positioning the VG at 25%c on the symmetric NACA 0021 airfoil yields a marked decrease in drag coefficient, accompanied by a significant improvement in lift performance, thereby contributing to stall delay.

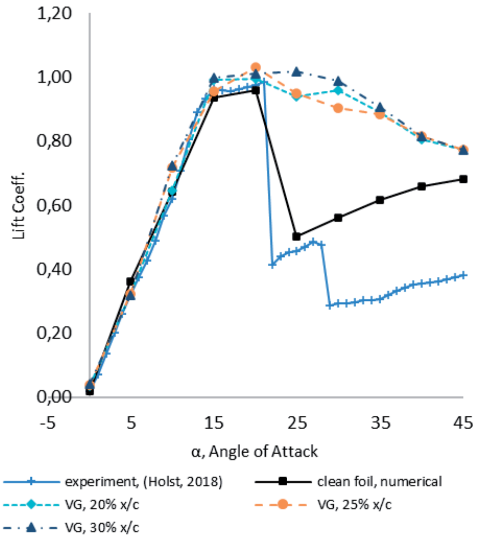

Fig. 5. Lift Coefficient of the NACA 0021 foil

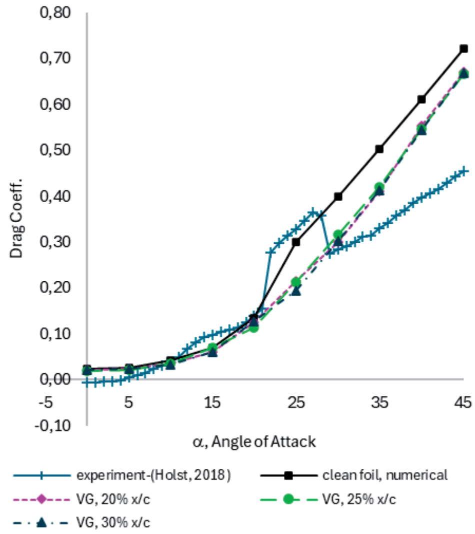

Fig. 6. Drag Coefficient of the NACA 0021 foil

3.2 The lift-to-drag (C_L/C_D) ratio

The C_L/C_D ratio is basically used to understand the shape when interacting with fluid. The coefficient of the C_L/C_D ratio significantly influences the energy efficiency of wind turbines by determining the optimal power coefficient. A higher C_L/C_D ratio allows for better hydrodynamic performance, leading to increased power output. C_L represents how much useful force is generated, like the upward force on a wing or the driving force on a turbine blade. Meanwhile, C_D represents the resistance that tries to slow everything down.

The C_L/C_D ratio tells us how efficiently a shape converts fluid flow into useful force compared to how much energy is lost to drag. A high C_L/C_D ratio means the design generates a lot of lift with little drag. This is what engineers prefer, as it means better performance and less wasted energy. On the other hand, a low ratio means the profile performs poorly.

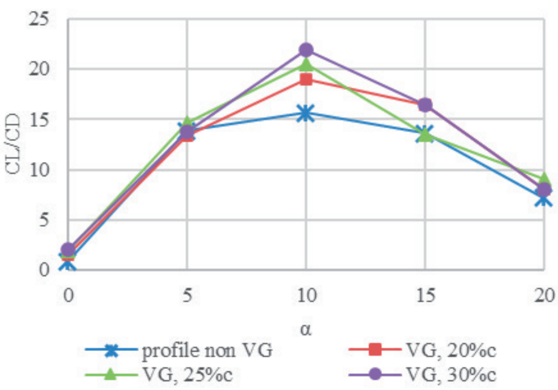

Fig. 7. Ratio C_L/C_D

This **Fig. 7** compares the hydrodynamic efficiency (C_L/C_D) of a standard wing profile against those equipped with VGs at various angles of attack (α). Overall, the addition of VGs consistently enhances the wing's performance across all angles, with peak efficiency for every configuration occurring at a 10°. Among the tested variations, placing the VG at the 30% position yields the most optimal results, achieving the highest lift-to-drag ratio compared to the baseline profile and other VG placements.

The C_L/C_D ratio improves when VGs are added to the original profile. The most noticeable improvement occurs when the VGs are placed at 30%c, resulting in a 21.4% increase. When positioned at 25%c, the ratio increases by 16.5%, while placement at 20%c leads to a 14.2% improvement. Overall, these results show that the position of the VGs plays an important role in enhancing hydrodynamic efficiency, with the 30%c position giving the best performance among the cases studied.

3.3 Velocity field

Fig. 8 illustrates the velocity magnitude contours around the airfoil for angles of attack ranging from $\alpha = 0°$ to 45°, comparing the profile with and without VG. The contour levels represent the local flow velocity, where low-velocity regions (blue) indicate flow deceleration and potential separation, while higher velocities (green to yellow) correspond to accelerated flow regions.

At low angles of attack ($\alpha \leq 10°$), the flow remains predominantly attached over the airfoil surface for both configurations. The velocity distribution is nearly identical, indicating that the inclusion of VG does not significantly influence the flow field in the pre-separation regime. This is expected, as the boundary layer retains sufficient momentum to resist adverse pressure gradients.

As the angle of attack increases to moderate values ($15° \leq \alpha \leq 25°$), the onset of flow separation becomes evident in the baseline configuration. This is characterized by the emergence and downstream growth of a low-velocity region on the suction side. In contrast, the VG-equipped airfoil exhibits a noticeably reduced separated region. The presence of VG enhances momentum exchange within the boundary layer, thereby delaying separation and maintaining a more attached flow.

At higher angles of attack ($\alpha \geq 30°$), the disparity between the two configurations becomes substantial. The baseline airfoil develops a large separated flow region accompanied by an extensive low-velocity wake, indicating significant flow detachment and degraded aerodynamic performance. Conversely, the VG configuration demonstrates a more confined separation zone and a comparatively narrower wake. Although separation is not entirely suppressed, its spatial extent and intensity are clearly mitigated.

Overall, the results confirm that VGs are effective in delaying flow separation and reducing wake development under high-angle-of-attack conditions. This flow control mechanism contributes to improved aerodynamic characteristics, particularly in sustaining lift and limiting drag increase in the near-stall and post-stall regimes.

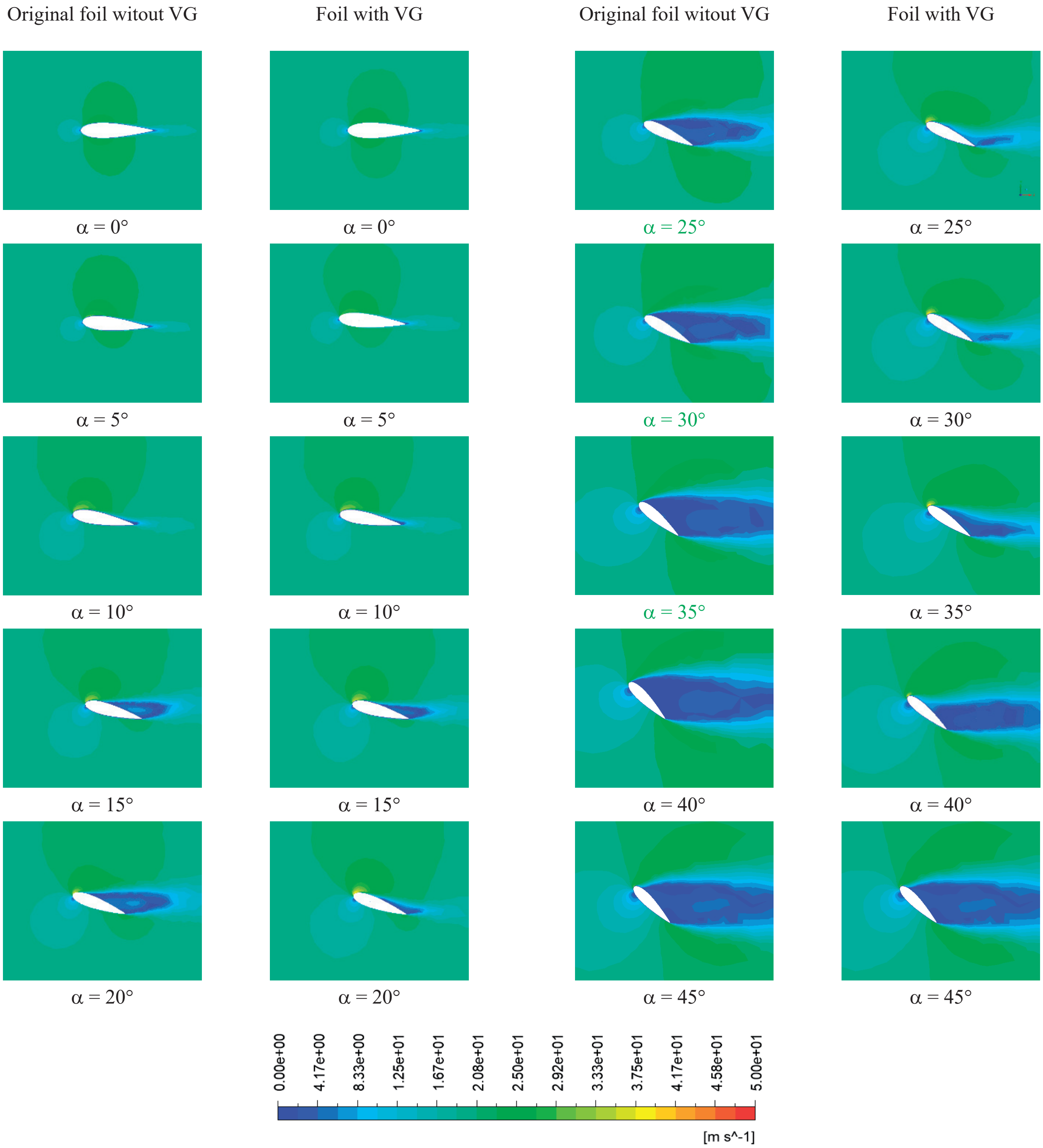

Fig. 8. Velocity magnitude at different AoA for both, profile without and with VGs at 25%c.

At higher angles of attack ($\alpha \geq 30°$), the baseline airfoil experiences extensive flow detachment, resulting in a large wake region and significant aerodynamic degradation. This is typically associated with a sharp decline in C_L/C_D. Conversely, the VG-equipped airfoil maintains a relatively more attached flow, with a smaller separation region and a more confined wake. This explains the ability of the VG configurations to sustain higher C_L/C_D values even in near-stall and post-stall conditions.

Overall, the contour visualization provides clear physical insight into the aerodynamic performance trends. The reduction in separation and wake size induced by VG leads to improved flow attachment, which directly translates into higher C_L/C_D. Therefore, the observed performance gains are not only quantitative but also strongly supported by the underlying flow physics.

When intermediate angles of attack ($15° \leq \alpha \leq 25°$) are reached, the airfoil not using VG starts developing flow separation on the intake side, which can be seen from the emergence of a low-speed zone. On the other hand, the VG case demonstrates separation delay along with a smaller size. This effect is tightly related to the rise of C_L/C_D ratio values, since it is evident that the case with VG provides an increment in C_L/C_D equal to about 14.2% (20%c), 16.5% (25%c), and 21.4% (30%c) relative to the case without VG.

For a steady, incompressible, and frictionless flow along a streamline, Bernoulli's principle holds that the sum of the fluid's static pressure, its velocity-dependent (dynamic) pressure, and its elevation (hydrostatic) pressure remains invariant:

$$p + 0.5\,\rho v^2 + \rho g h = constant \tag{6}$$

In this expression, p represents the static pressure, ρ the density, v the flow speed, g the acceleration due to gravity, and h the height above a chosen reference. Thus, regions of higher flow velocity correspond to lower static pressure (and vice versa), reflecting the fluid's mechanical energy conservation.

Along an airfoil, the flow speeds up over the curved upper surface and slows down along the lower surface. By Bernoulli's principle, wherever the fluid velocity, v increases, the static pressure, p decrease so that constant along a given streamline. If it compares two streamlines-one just above the airfoil (speed, v_{top}) and one just below (speed, v_{bottom}). Since $v_{top} > v_{bottom}$, the pressure on the upper surface is lower than that on the lower surface. This net pressure difference integrated over the foil's planform produces lift, which is the fundamental mechanism by which an airfoil generates the force. This result underpins devices and phenomena such as airfoil lift.

This is attributed to the vortices generated by the VGs, which follow a curved or helical trajectory downstream along the surface while transporting high-energy fluid from the free stream into the near-wall region. This momentum exchange helps delay separation by energizing the boundary layer. However, as the vortex convects downstream, it gradually decays due to viscous diffusion and interaction with surrounding flow structures. The rate of decay depends on factors such as the VG geometry, Reynolds number, and boundary layer characteristics [36]. A well-designed VG ensures that the vortex remains coherent over a sufficient length to maintain flow attachment in critical regions of the airfoil.

3.4 VG integration increases turbine power with a theoretical approach.

The integration of VGs into a (VACT) based on simulation data and simplified calculations requires several assumptions. This approach is intended solely to obtain a preliminary prediction of the impact of VG integration on the VACT's performance. In general, achieving more accurate predictions requires further simulations involving the entire rotating turbine to comprehensively explore its overall behavior.

Fig. 9 shows the change in a single blade's speed vector over a single rotation. Even with constant rotating speed and wind speed, the resultant velocity and AoA vary in both direction and amplitude with azimuth angle. The upstream half-cycle ($0° < \theta < 180°$) of the bar is positive, whereas the downstream half-cycle ($180° < \theta < 360°$) is negative.

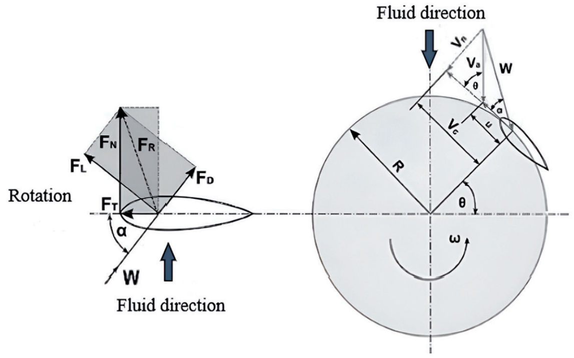

Fig. 9. Force and velocity vectors of a VAT [39]

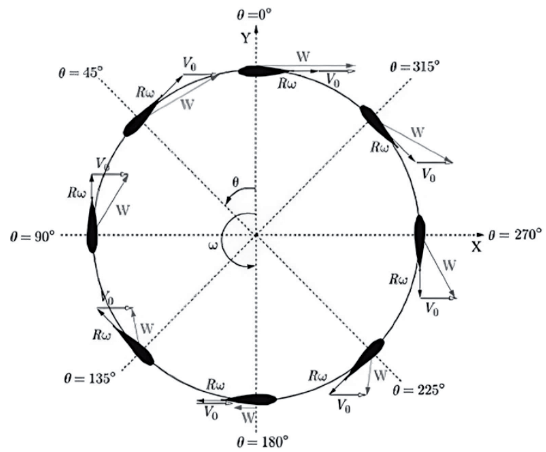

Fig. 10. Velocity vectors at different azimuth angles [43]

The hydrodynamic performance of vertical-axis turbines is characterized by complex flow phenomena, including cyclic variations in the angle of attack, dynamic stall effects, and strong flow interference between the upwind and downwind passes of the blades (**Fig. 10**). To address these challenges and to provide a computationally efficient predictive tool, Paraschivoiu, (2002) developed the Double-Multiple Stream Tube (DMST) theory, an extension of the classical momentum and blade element theories, specifically tailored for Darrieus-type vertical axis turbines [37].

The fundamental principle of the DMST model is based on dividing the turbine's swept area into several independent stream tubes, each representing a discrete section of the flow field. Within each stream tube, the conservation of momentum is applied separately to the upwind and downwind regions of the turbine, hence the term double stream tube. This dual treatment allows for distinct induced velocity distributions in both regions, reflecting the fact that the downstream flow has already been influenced by the energy extraction occurring in the upwind half.

Each stream tube is analyzed independently, and the interaction between the hydrodynamic forces generated by the blades and the local flow conditions is evaluated using a blade element approach. The local induced velocities are iteratively updated until the momentum balance between the air stream and the blade forces is satisfied. Through this iterative process, the model predicts the distribution of hydrodynamic loads, torque, and power coefficients across the turbine's azimuthal positions.

The logical flow of the analysis is as follows: L and D forces are first transformed into normal (C_N) and tangential (C_T) force components, which are then used to compute the elemental torque (Q). The elemental torque is integrated to obtain the total rotor torque (Q_{total}), from which the mechanical power (P) and the power coefficient (C_p) are subsequently determined.

$$C_N = C_L \cos\alpha + C_D \sin\alpha \tag{7}$$

$$C_T = C_L \sin\alpha - C_D \cos\alpha \tag{8}$$

The relative inflow velocity (W) results from the vector combination of the local velocity (V) and the blade's tangential velocity due to rotor rotation ($R\omega$). Because the blade's direction of motion changes with azimuthal position, the magnitude of W varies over one revolution and directly governs the angle of attack (α) and the resulting aerodynamic forces on the blade.

$$\overrightarrow{W} = \vec{V} + \overrightarrow{R\omega} \tag{9}$$

The elemental torque (Q) generated by a blade element at a radial position (r) is obtained from the product of the elemental thrust force and the moment arm. By substituting the expression for the thrust force, the elemental torque can be written accordingly.

$$dQ(\theta) = r\,\frac{1}{2}\rho W^2(\theta)\,c\,\frac{C_T(\theta)}{\cos\delta(\theta)}\,dz \tag{10}$$

Since W, C_T, and δ are functions of the blade azimuthal angle (θ), the torque produced by the blade varies over one full revolution of the rotor.

The total torque generated by a single blade is obtained by integrating the elemental torque along the blade height. Subsequently, to determine the average torque over one full revolution, an integration is performed with respect to the blade's azimuth angle from 0 to 2π. For a rotor with blades number (N_b), the total torque (Q_{total}) is expressed as the summation of contributions from all blades

$$Q_{\text{total}} = N_b\,\bar{Q} \tag{11}$$

Mechanical power (P_m) produced by the rotor is subsequently determined by the product of total torque and angular velocity (ω):

$$P_m = Q_{\text{total}}\,\omega \tag{12}$$

Maximum kinetic power of the fluid (P) is:

$$P = \frac{1}{2}\rho A V_\infty^3 \tag{13}$$

VACTs type-H usually uses a symmetrical profile as a turbine blade part because of its ability to maintain lift performance on both sides of the blade when the turbine rotates. NACA 0021 is a symmetrical blade profile with a maximum thickness of 21% chord at 30% chord from the leading edge. This profile also has a peak C_l value of 0.98 [6]. In this study, VGs are applied to foils to investigate their functional effects between foils without and with VGs. The applied VGs are rectangular single-row VG arrays and counter-rotating configurations.

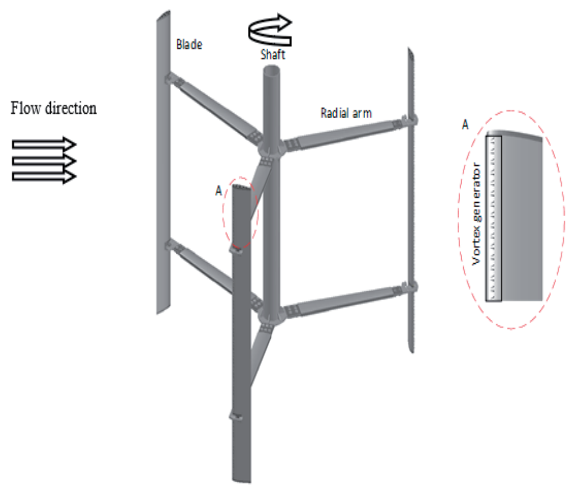

Fig. 11. Vertical axis current ocean turbine, H-darrieus type with VGs

Meanwhile, augmentation devices are used to alter the fluid flow behaviour around VACTs type-H by VG, where the VG is positioned on the blade surface in a configuration of a pair of VGs along the blade span, as represented in **Fig. 11.** The dimensions, positions, configurations, and types of airfoils determine the success of adding a VG in producing vortex flow with stall delay, increasing lift, and reducing drag. The Darrieus turbine, which drives the VACT, is a lift-driven device. Increasing lift performance is expected to improve turbine efficiency and self-starting capability.

Fig. 12. BRIN vertical-axis ocean current turbine prototype conducted in 2014 (BRIN-documents, 2014)

This section investigates the impact of VG installation on the variation of energy extracted by the VACT, which is assumed to harness hydrokinetic energy from ocean currents. **Fig. 12** illustrates the preparation activities for the field trial of the BRIN vertical-axis ocean current turbine prototype conducted in 2014. In this study, the turbine prototype corresponds to the BRIN marine current turbine previously tested in the Madura Strait, Indonesia. The turbine, equipped with NACA 0021 blades, has a diameter (D) of 3.6 m, a span (s) of 2.18 m, and a chord length (c) of 0.18 m. During field testing, the turbine operated under ocean current velocities (v) ranging from 0.6 to 1.10 m/s, with a cut-in speed of 0.6 m/s and a total power coefficient of 37% by Kasharjanto and Rahuna, (2017). Based on the field test conducted in the Madura Strait, Indonesia, the turbine generated 480 W of power at an ocean current velocity of 1.10 m/s [38].

In this study, it is demonstrated that integrating VGs with the turbine blades improves the flow characteristics around the blades, thereby increasing lift and reducing drag. The enhancement of lift contributes to stall delay and an increase in turbine torque, which ultimately leads to an improvement in the power performance of the vertical-axis marine current turbine. Based on the predicted power enhancement, the addition of square-type VGs results in a 7.5% increase in power output, yielding 518 W. The simulation outcomes demonstrate that positioning the VG at 25% chord on the symmetric NACA 0021 airfoil yields a marked decrease in drag coefficient, accompanied by a significant improvement in lift performance, thereby contributing to stall delay.

4. Conclusion

This study investigated the effect of rectangular VGs on the hydrodynamic performance of the NACA 0021 hydrofoil used in a Vertical Axis Current Turbine (VACT) through CFD simulation using the k–ω SST turbulence model at a Re. 1.917×10^5. The results show that the addition of VGs was able to improve the lift coefficient, reduce drag, delay flow separation, and enhance the overall hydrodynamic efficiency of the hydrofoil, especially at moderate to high angles of attack.

Among the tested configurations, the VG placed at 30%c produced the highest improvement in the lift-to-drag ratio (C_L/C_D), reaching 21.4% compared to the clean hydrofoil. Meanwhile, the VG located at 25%c provided the most significant drag reduction and demonstrated strong capability in delaying stall. Flow visualization also confirmed that the VGs helped maintain flow attachment and reduced wake formation behind the hydrofoil, particularly in near-stall and post-stall conditions.

The improved aerodynamic characteristics directly contributed to better turbine performance. Based on the theoretical prediction using the DMST approach, the integration of VGs on the VACT blade increased the estimated turbine power output from 480 W to 518 W, corresponding to a power enhancement of approximately 7.5%. These findings indicate that VGs are a promising and practical passive flow-control device for improving the performance and self-starting capability of vertical-axis marine current turbines.

Although the present work was limited to steady-state simulations on a single blade, the study provides important initial insights into the influence of VG placement on VACT performance. Future studies are recommended to include full rotating turbine simulations and unsteady flow analysis to better capture dynamic stall behavior and blade interaction effects under realistic operating conditions.

Acknowledgements

The first author specifically expressed his deepest appreciation to the National Research and Innovation Agency of the Republic of Indonesia which funded this project through a scheme called The Education of Degree by Research Doctoral Program, based on the decree of the Deputy for Human Resources in Science and Technology (SDM IPTEK), No. 27/II/HK/2024. This article is one of the targets that must be achieved in implementing the Degree by Research Doctoral Program. This research is also supported by the Research Implementation Program of the Organization Research for Energy and Manufacturing, National Research and Innovation Agency (BRIN), under Research Activity Grant No. 6/III.3/HK/2026.

References

[1] H. D. Taylor. (1947). The elimination of diffuser separation by vortex generators. *Res Dep Rep no r-4012-3, United Aircr Corp East Hartford, Connect*, vol. 103.

[2] X. K. Li, S. Kang, L. P. Dai, and J. D. Jiao. (2015). Effects on airfoil flow field by structure of vortex generators. *K Cheng Je Wu Li Hsueh Pao/Journal Eng Thermophys*, vol. 36, no. 2, pp. 326–329.

[3] S. Georgilidakis. (2022). NASA Puts New Twist on Vortex Generators? https://mentourpilot.com/nasa-puts-new-twist-on-vortex-generators/

[4] Z. Zhao, D. Wang, T. Wang, W. Shen, H. Liu, and M. Chen. (2022). A review: Approaches for aerodynamic performance improvement of lift-type vertical axis wind turbine. *Sustain*

Energy Technol Assessments, vol. 49. doi: 10.1016/J.SETA.2021.101789.

[5] M. Manolesos and S. G. Voutsinas. (2015). Experimental investigation of the flow past passive vortex generators on an airfoil experiencing three-dimensional separation. *J Wind Eng Ind Aerodyn*, vol. 142, pp. 130–148. doi: 10.1016/j.jweia.2015.03.020.

[6] D. Holst, B. Church, F. Wegner, G. Pechlivanoglou, C. N. Nayeri, and C. O. Paschereit. (2019). Experimental Analysis of a NACA 0021 Airfoil under Dynamic Angle of Attack Variation and Low Reynolds Numbers. *J Eng Gas Turbines Power*, vol. 141, no. 3. doi: 10.1115/1.4041146.

[7] A. Saenz-Aguirre, U. Fernandez-Gamiz, E. Zulueta, I. Aramendia, and D. Teso-Fz-Betono. (2022). Flow control based 5 MW wind turbine enhanced energy production for hydrogen generation cost reduction. *Int J Hydrogen Energy*, vol. 47, no. 11, pp. 7049–7061. doi: 10.1016/J.IJHYDENE.2020.01.022.

[8] B. K. Kirke and L. Lazauskas. (2011). Limitations of fixed pitch Darrieus hydrokinetic turbines and the challenge of variable pitch. *Renew Energy*, vol. 36, no. 3, pp. 893–897. doi: 10.1016/J.RENENE.2010.08.027.

[9] M. J. Khan, G. Bhuyan, M. T. Iqbal, and J. E. Quaicoe. (2009). Hydrokinetic energy conversion systems and assessment of horizontal and vertical axis turbines for river and tidal applications: A technology status review. *Appl Energy*, vol. 86, no. 10, pp. 1823–1835. doi: 10.1016/j.apenergy.2009.02.017.

[10] Erwandi *et al.* (2013). Turbin Type Darrieus Poros Vertikal dengan Menggunakan Sudut Serang Pasif yang Fleksibel. IDP000035145.

[11] R. Hantoro, I. K. A. P. Utama, Erwandi, and A. Sulisetyono, “An experimental investigation of passive variable-pitch vertical-axis ocean current turbine,” *ITB J Eng Sci*, vol. 43 B, no. 1, pp. 27–40, 2011, doi: 10.5614/itbj.eng.sci.2011.43.1.3.

[12] D. Satrio and I. K. A. P. Utama. (2023). Experimental investigation into the improvement of self-starting capability of vertical-axis tidal current turbine. *Elsevier*. doi: 10.1016/J.EGYR.2021.07.027.

[13] E. M. Suyanto, S. P. Fitri, Erwandi, D. Rahuna, and A. Kasharjanto. (2023). Experimental Study of the Influence Wave Period on the Performance Darrieus Turbine with Modification of the Blade Angle,” *IOP Conf Ser Earth Environ Sci*, vol. 1166, no. 1. doi: 10.1088/1755-1315/1166/1/012020.

[14] D. Rahuna, Erwandi, A. Kasharjanto, E. M. Suyanto, and C. S. J. Mintarso. (2023). Experimental Study on Hydrodynamic Aspects of Turbine which Convert Hydrokinetic and Potential Coastal Wave Energy. *IOP Conf Ser Earth Environ Sci*, vol. 1166, no. 1. doi: 10.1088/1755-1315/1166/1/012021.

[15] W. Xu, G. Li, F. Wang, and Y. Li. (2020). High-resolution numerical investigation into the effects of winglet on the aerodynamic performance for a three-dimensional vertical axis wind turbine. *Energy Convers Manag*, vol. 205, no. December 2019. doi: 10.1016/j.enconman.2019.112333.

[16] L. Zhang, X. Li, K. Yang, and D. Xue. (2016). Effects of vortex generators on aerodynamic performance of thick wind turbine airfoils. *J Wind Eng Ind Aerodyn*, vol. 156, pp. 84–92. doi: 10.1016/J.JWEIA.2016.07.013.

[17] W. Miao, Q. Liu, Z. Xu, M. Yue, C. Li, and W. Zhang. (2022). A comprehensive analysis of blade tip for vertical axis wind turbine: Aerodynamics and the tip loss effect. *Energy Convers Manag*, vol. 253, no. September 2021, p. 115140. doi: 10.1016/j.enconman.2021.115140.

[18] S. M. H. Karimian and A. Abdolahifar. (2020). Performance investigation of a new Darrieus Vertical Axis Wind Turbine. *Energy*, vol. 191, p. 116551. doi: 10.1016/j.energy.2019.116551.

[19] D. Satrio *et al.* (2023). Effect of Positioning a Circular Flow Disturbance in front of the Darrieus Turbine. *IOP Conf Ser Earth Environ Sci*, vol. 1166, no. 1. doi: 10.1088/1755-1315/1166/1/012019.

[20] D. Satrio, Suntoyo, and L. I. Ramadhan. (2022). The advantage of flow disturbance for vertical-axis turbine in low current velocity. *Sustain Energy Technol Assessments*, vol. 49. doi: 10.1016/j.seta.2021.101692.

[21] M. B. Salleh, N. M. Kamaruddin, and Z. Mohamed-Kassim. (2021). The effects of a deflector on the self-starting speed and power performance of 2-bladed and 3-bladed Savonius rotors for hydrokinetic application. *Energy Sustain Dev*, vol. 61, pp. 168–180. doi: 10.1016/j.esd.2021.02.005.

[22] D. De Tavernier, C. Ferreira, A. Viré, B. LeBlanc, and S. Bernardy. (2020). Controlling dynamic stall using vortex generators on a wind turbine airfoil,” *Renew Energy*, vol. 172, pp. 1194–1211, 2021, doi: 10.1016/j.renene.2021.03.019.

[23] I. K. A. P. Utama *et al.* (2020). Numerical simulation of foil with leading-edge tubercle for vertical-axis tidal-current turbine,” *J Mech Eng Sci*, vol. 14, no. 3, pp. 6982–6992. doi: 10.15282/jmes.14.3.2020.02.0547.

[24] D. Rahuna, Erwandi, D. Satrio, and I. K. A. P. Utama. (2024). Opportunities for Utilizing Vortex Generators on Vertical Axis Ocean Current Turbines: A Review. *BIO Web Conf*, vol. 89. doi: 10.1051/bioconf/20248910003.

[25] D. Satrio, Erwandi, and D. Rahuna. (2025). Investigation of enhanced peak lift performance and stall angle delay by attachment of Vortex Generators on blade surfaces of Vertical Axis Ocean Current Turbine. *Ocean Eng*, vol. 326, p. 120762. doi: 10.1016/J.OCEANENG.2025.120762.

[26] L. Galera, P. Martinez-Filgueira, U. Fernández-Gámiz, E. Zulueta, J. M. Lopez, and J. M. Blanco. (2019). A triangular vortex generator modeling on a DU97-W-300 airfoil by a source term model,” *Proc Inst Mech Eng Part A J Power Energy*, vol. 233, no. 5, pp. 635–645. doi: 10.1177/0957650919850449.

[27] H. Müller-Vahl, G. Pechlivanoglou, C. Nayeri, and C. Paschereit, *Vortex Generators for Wind Turbine Blades: A Combined Wind Tunnel and Wind Turbine Parametric Study*, vol. 6. 2012. doi: 10.1115/GT2012-69197.

[28] D. Baldacchino, C. Ferreira, D. De Tavernier, W. A. Timmer, and G. J. W. van Bussel. (2018). Experimental parameter study for passive vortex generators on a 30% thick airfoil: Experimental parametric vortex generator study. *Wind Energy*, vol. 21, no. 9, pp. 745–765. doi: 10.1002/WE.2191.

[29] H. Wang, B. Zhang, Q. Qiu, and X. Xu. (2017). Flow control on the NREL S809 wind turbine airfoil using vortex generators,” *Energy*, vol. 118, pp. 1210–1221. doi: 10.1016/j.energy.2016.11.003.

[30] B. Wei, Y. Gao, and S. Hu. (2023). Experimental Study on Multiobjective Flow Control of Dynamic Stalls Using a Vortex Generatorle. *J Aerosp Eng*, vol. 36, no. 6. doi: https://doi.org/10.1061/JAEEEZ.ASENG-4989.

[31] F. M. Kale, N. Yilmaz, K. F. Sokmen, and W. Shi. (2025). Experimental and numerical investigations of hydrodynamic

performance for horizontal-axis hydrokinetic turbines. *Brodogradnja* vol. 76, no. 3.

[32] W. Shi, M. Atlar, R. Norman, B. Aktas, and S. Turkmen. (2016). Numerical optimization and experimental validation for a tidal turbine blade with leading-edge tubercles. *Renew Energy*, vol. 96, pp. 42–55. doi: 10.1016/J.RENENE.2016.04.064.

[33] M. I. Zafar, M. M. Choudhari, P. Paredes, and H. Xiao. (2021). Recurrent neural network for end-to-end modeling of laminar-turbulent transition. doi: 10.1017/dce.2021.11.

[34] Y. Yan, E. Avital, J. Williams, and J. Cui. (2019). CFD analysis for the performance of micro-vortex generator on aerofoil and vertical axis turbine. *J Renew Sustain Energy*, vol. 11, no. 4. doi: 10.1063/1.5110422.

[35] ITTC. (2017). The Specialist Committee on CFD and EFD Combined Methods Final Report and Recommendations to the 29th ITTC. *ITTC – Recomm Proced Guidel Guidel Spec Comm CFD EFD Comb Methods*, pp. 1–8. https://ittc.info/media/9098/sc-combined-cfd-efd-methods.pdf

[34] J. C. Lin. (2002). Review of research on low-profile vortex generators to control boundary-layer separation. *Pergamon*. doi: 10.1016/S0376-0421(02)00010-6.

[35] N. Troldborg, F. Zahle, and N. N. Sørensen. (2015). Simulation of a MW rotor equipped with vortex generators using CFD and an actuator shape model. *53rd AIAA Aerosp Sci Meet*, no. January, pp. 1–10. doi: 10.2514/6.2015-1035.

[36] A. Kasharjanto, D. Rahuna, and D. Rina. (2017). Kajian Pemanfaatan Energi Arus Laut Di Indonesia - Study on the Implementation Of Marine Current Energy In Indonesia. *Jurnal Ilmiah Teknologi Maritim*, vol. 11, no. 2, pp. 75–84. (in Indonesia language).

---

x\F. Aleotti[1], A. Rollo[1,], P. Marcolin[1], V. Angelucci[1], D. Cilio[1], M. Zulianello[1],*

A new smart charging strategy for electric vehicles in energy communities: An Italian case study

[1]Ricerca sul Sistema Energetico – RSE s.p.a., Via R. Rubattino 54, 20134 Milano
*Corresponding author: federico.aleotti@rse-web.it

Original scientific paper
Received: December 23, 2025
Accepted: July 1, 2026
https://doi.org/10.65776/ep.21.1.2

Abstract

The aim of this study is to evaluate the energy and economic benefits of different Electric Vehicles (EV) charging strategies within Renewable Energy Communities (REC) in Italy. The electrification process for mobility purposes will lead to increased and concentrated electricity demand that may lead to network congestion and other issues. Distributed self-consumption combined with RECs and optimal control of EVs' charging profiles may reduce the network stress and improve the economic benefits of stakeholders. A simulated case study is used to explore three cases in which 20 EVs (domestic and commercial): (i) are charged independently using a "standard" charging strategy, (ii) join a REC with other users and there aren't modifications of EV charging profiles, (iii) implement smart charging strategies to integrate with the REC via real-time control infrastructure. In this last case, EV charging power is controlled by a remote controller that monitors the production and consumption of all REC members and controls the EV charge to maximize energy sharing while respecting infrastructure and users' constraints (e.g., guarantees of minimum SOC, EV maximum charging power, etc.). The developed algorithm firstly simulates all EV trips in a year starting from probability distributions for different parameters, recreating their location and availability for charging on a 15min timestep granularity; secondly, it computes the REC energy flows and assigns the charging power to all vehicles, based on the charging logic which changes across the cases. In conclusion, the paper shows how the EV smart charging and load shift can generate additional value in the form of incentives (+50%) to the REC, without creating disruptions in terms of mobility.

Keywords: *Renewable Energy Community (REC), Electric Vehicles, Load Shifting, Smart Charging, Shared Energy, Italian Policy*

1. Introduction

The European Union has set the objective of achieving climate neutrality by 2050. To enable this energy transition, the *European Green Deal* proposes a series of legislative reforms. Its key objectives include reducing greenhouse gas emissions, increasing the share of renewable energy, promoting electrification, and enhancing energy efficiency. The central element of this strategy is *empowerment and consumer engagement*; the aim is to raise end-user awareness, facilitate access to information, and encourage active participation. For this purpose, new consumption models such as Energy Communities have been introduced at European level thanks to the *Clean Energy for All Europeans Package*. This package includes the *RED II Directive (2018/2001)* [1], which introduced the concept of Renewable Energy Communities (REC), and *Directive 2019/944* [2], which established Citizens' Energy Communities (CEC). According to the *RED II Directive*, a REC is a legal entity based on open and voluntary participation by individuals, small and medium-sized enterprises (SMEs), or local authorities located in proximity to renewable energy plants. Its primary purpose is not the financial profit, but the generation of environmental, economic, and social benefits for its members and the local community. In Italy, the *RED II Directive* was implemented in two phases: an experimental phase with *Legislative Decree 162/2019* [3] and an operative phase with *Decree-Law 199/2021* [4] with the full transposition of the RED II. The key aspects such as the incentive tariff for shared energy, the funds of the *National Recovery and Resilience Plan* (PNRR), and the requirements for accessing the incentives are defined in the *Integrated Text for Diffused Self-Consumption* (TIAD) published by the *Regulatory Authority for Energy, Networks and the Environment* [5], the *Ministry Decree 414/2023* which regulates the incentives [6] and the Operating Rules issued by the *Gestore Servizi Energetici* (GSE) [7]. The legislation was subsequently updated to clarify certain provisions and to broaden access to PNRR funding. Italian legislation has introduced three specific configurations for renewable energy sharing, known as *Self-Consumption Configurations for Renewable Energy Sharing* (CACER):

- **Renewable Energy Communities (REC):** members share energy "virtually" through the national distribution grid.
- **Group of Renewable Energy Self-Consumers Acting Collectively:** all members and systems are located within the same building or condominium.
- **Individual Remote Self-Consumers of Renewable Energy:** a single end customer produces renewable energy for their own consumption using systems that are not physically connected to their point of delivery.

The GSE incentivizes virtually shared energy in these configurations for 20 years, with a premium tariff that varies between approximately €80 and €130/MWh, depending on plants' capacities.

The empowerment of end consumers through these new consumption models aims to promote a more intelligent use of electricity and a more efficient use of the grid. In recent decades there has been a growing diffusion of distributed generation systems, and the electricity sector has undergone a deep transformation, moving from a *centralized generation model* (with a few large-scale power plants located "upstream" of the grid) to a *decentralized generation model* (with many small-scale plants distributed across the grid) [8]. These "distributed" generation plants mainly exploit renewable sources, in particular photovoltaic systems [9]. Photovoltaic generation plants have a "bell-shaped" production curve where the production is concentrated in the central hours of the day. However, the electricity consumption follows an inverse trend, peaking in the late afternoon and evening hours. This temporal mismatch between generation and consumption can lead to several problems, such as difficulty in managing new bidirectional power flows, voltage and frequency variations, overheating and consequent cable deterioration, and the well-known "*Duck Curve*" effect [10]. These phenomena can lead to greater grid instability, progressive deterioration of cables and protection devices, lower quality of service, etc. To ensure proper functioning of the electrical system, it is therefore necessary to invest in modernizing the national grid by developing the *smart grid paradigm* [11] and, at the same time, encourage more conscious electricity use by end consumers. Load management techniques such as load shifting allow part of consumption to be shifted to photovoltaic generation peak hours with consequent benefits for the electrical system. These load management techniques should be applied in sectors with a minimum level of consumption flexibility, such as domestic sector (in this case, flexible loads are, for example, washing machines and dishwashers). The effects on the electricity system caused by load shifting of flexible household appliances have already been studied [12]. That research highlighted the impacts on the grid promoted through different load management methodologies within a REC, in particular: (i) *Demand Side Engagement*, which involves spontaneous shifting of consumption by household users; and (ii) *Optimal Demand Side Management*, which involves optimized shifting of flexible loads to maximize the shared energy within the configuration. The impact of load shifting was analysed from both an energetic and economic prospective. The results highlighted how load management techniques can favour greater revenues deriving from incentives and from greater direct self-consumption of the energy produced by the systems. Within this study, however, the potential of storage systems and electric vehicles (EVs) to generate greater flexibility of final consumption was not evaluated. Several researchers have attempted to quantify the benefits generated by smart management of EV charging. Karameros et al. [13] analysed the environmental and economic impacts promoted by applying a "hybrid" optimization algorithm based on a Hierarchical Analytical Process and a genetic algorithm in a microgrid. An optimization algorithm is proposed, where buildings, photovoltaic plants, storage systems, and EVs (utilization of Vehicle to Grid technology, V2G) can efficiently meet the energy requirements and peak-hour energy demand, in both economic and sustainability terms. Moura et al. [14] investigated the increase in shared self-consumption and the reduction in electricity costs enabled by smart management of EVs in a case study located in Portugal. In this study, an optimization methodology was applied to correctly schedule EVs charging with vehicles managed at a "community" level. The results show a significant reduction in costs and increased local self-consumption of renewable energy under a "community based" EV management strategy compared to an "individual" management strategy for each building. Marcolin et al. [15] analysed various smart charging strategies for EV charging profile scheduling based on data from a real workplace infrastructure. By applying a MILP–based control algorithm, they demonstrated the potential to significantly mitigate system-level impact of EV charging, achieving a 40% reduction of total energy consumption from the grid and a 70% decrease in peak demand, without causing any incomplete charging events for end users and while generating operating cost savings ranging between 33% and 70% depending on the considered case.

The international literature on EV smart charging mainly frames charging control as an optimization problem aimed at reducing costs, limiting grid impacts, or increasing renewable self-consumption, often using forecasts of PV generation, demand, prices, or vehicle availability. However, real-time approaches have also been proposed to control EV charging directly from currently observed system conditions. Shern et al. [16] are one example of real-time EV smart control based on AI-based demand response relying on load and generation forecasting.

Despite this progress, existing research still pays limited attention to approaches that reduce reliance on AI, forecasting algorithms, and historical data. An example is represented by Wang et al. [17], which proposed a carbon-aware EV charging flexibility model which uses a Lyapunov prediction-free optimization responsive to grid carbon intensity. Forecasting-free approaches are relevant for REC applications too, where heterogeneous users, uncertain mobility patterns, and limited observability can make forecast-based scheduling difficult or expensive to implement. Accordingly, this paper evaluates a transparent real-time rule-based methodology for distributed self-consumption within a REC, in which the activation logic relies only on real-time consumption and generation. Instead of scheduling EV charging in advance or solving a forecast-based objective function, the controller estimates the current shared energy potential of the community and allocates charging power among connected EVs according to SOC, charging-station limits, contractual power constraints, and user-comfort thresholds. The novelty of the study therefore lies in assessing whether a forecast-free and objective-function-free control logic can still provide measurable energy and economic benefits, bridging the gap between highly optimized scheduling models and implementable REC-level control architectures.

2. CASE STUDY

The objective of this analysis is to assess the energy and economic benefits achievable through smart control of EV charging within a REC located in Italy, while proving whether a low technology and prediction-free algorithm can meet the users' needs in terms of EV charge availability for mobility demand. Accordingly, the calculation of revenues refers to the current Italian regulatory framework, considering the incentive to the amount of energy shared within the Energy Community [5]. The analysis highlights variation in energy self-consumption levels, both in terms of energy directly self-consumed at the user's point of delivery (i.e., *directly self-consumed energy*) and in terms of energy "virtually" shared within the Energy Community (i.e., *shared energy*). Increased direct self-consumption of electricity from photovoltaic systems results in electricity bill savings, while increased shared energy generates additional revenues for the REC due to higher incentive.

It is observed that in the domestic sector, users who own an EV tend to recharge frequently outside the generation hours of photovoltaic systems [18]. In fact, these users often use their cars for commuting, meaning that during the central hours of the day the EV is not connected to the charging station (CS). Conversely, a company with a fleet of EVs that does not operate on weekends has greater charging flexibility [15]. In fact, on holidays the EVs are connected to the CSs but since there is no need to complete the charging quickly, the charging power can be controlled to maximize the energy shared within the Energy Community. This paper proposes a control algorithm which reduces the EV fast charging in favor of more flexible, incentive-driven, forecast-free and low-power recharge without occurring in service disruptions. Further details will be provided later regarding the modelling of the state of charge (SOC) of EVs, patterns of vehicle use, and the methodology adopted to control charging power with the aim of increasing shared energy within the Community. Based on these considerations, an Energy Community was modelled in which a company equipped with a PV system for self-consumption and a fleet of Commercial Electric Vehicles (CEVs) participates alongside various domestic users with different characteristics, who also own Domestic Electric Vehicles (DEVs). The following case studies have been identified:

- **Reference Case (i.e. Ref Case):** This scenario assesses the energy expenditure and energy flows of the configuration in its current state without the establishment of a REC (therefore, there are no revenues related to the incentive) and without the smart control of EV charging. Photovoltaic generation systems and EVs are still considered in this configuration. Table 1 summarizes the number of users by type, the capacity of the generation systems, the capacity of the storage systems and the number of EVs. The reported values for the various parameters refer to individual users. Therefore, there are users (domestic and commercial) who self-consume energy from generation plants (prosumers) and users who own an electric vehicle. The latter typically charge their vehicles based on their needs, always maintaining a minimum charging rates and without any smart charging control. Since there is no REC, there are no revenues linked to the incentives applied to the shared energy. It is assumed that the commercial user has two points of delivery: a main point of delivery (i.e., *main POD*) to which all loads and the photovoltaic generation plant are connected, and a secondary point of delivery dedicated solely to the charging infrastructure (i.e., *CSs POD*). It is assumed that the number of CSs equals the number of cars in the company fleet (a total of 10 CSs). Domestic users who own generation plants are also equipped with electric storage systems.

Table 1. Characteristics of the analyzed configuration.

ID	Typology user	Number	Contractual power [kW]	PV	PV capacity [kW]	Storage capacity [kWh]	EV	EV Number
Prosumer	Commercial	1	100	Yes	300	0	No	-
Charging stations	Commercial	1	500	No	-	-	Yes	10
HH	Domestic	5	6	No	-	-	No	-
HH_PV	Domestic	5	6	Yes	6*	10*	No	-
HH_EV	Domestic	5	6	No	-	-	Yes	1*
HH_PV_EV	Domestic	5	6	Yes	6*	10*	Yes	1*

*For each user

- **Renewable Energy Community Case (i.e. REC Case):** Compared to the Reference Case, there are no changes to the configuration, the same characteristics and number of users are reported in Table 1. However, in this case, users participate in a REC and benefit from the revenues associated with the incentive on energy virtually shared through the electricity grid. Consequently, revenues and thus energy expenditure for each individual user change. No modifications are applied to EV charging strategies, and the charging profiles remain unchanged compared to the Reference Case The only variations occur in economic flows: the REC introduces a new revenue stream and additional cost items for both the initial investment and operating costs, while energy flows remain unchanged. All assumptions regarding the systems and the commercial user's points of delivery also remain the same. All assumptions regarding the systems and the commercial user points of delivery also remain unchanged.
- **Renewable Energy Community and Smart Charging Case (i.e. REC – SC Case):** Once again, there are no changes to the configuration; the same characteristics and number of users are reported in Table 1. In this case, users also participate in REC and benefit from the revenues associated with shared energy incentives. However, the charging profiles of EVs differ, and a "smart" charging strategy is applied to maximize the energy shared by the REC at any given time. Further details on the smart charging strategy are provided in the following sections. Smart control of EVs entails higher initial investment costs as well as higher operating costs related to measurement instruments, control tools, management platform, and so on. However, these extra costs and details on hardware and software of the controlling equipment are not in the scope of this study.

The assumptions made for the various cases analyzed are summarized in Table 2.

The characteristics of the EVs and charging infrastructure simulated in this study are summarized in Table 3.

Table 2. Summary of the hypothesis for the different cases.

Cases	Photovoltaic plants	Vehicles electric	Energy Community	Smart charging for EVs
Reference Case (Ref Case)	Yes	Yes	No	No
Renewable Energy Community Case (REC Case)	Yes	Yes	Yes	No
Renewable Energy Community and Smart Charging Case (REC - SC Case)	Yes	Yes	Yes	Yes

Table 3. Characteristics of EVs and charging stations.

Variable	Domestic EV – DEV	Commercial EV - CEV
Vehicle type	Multi-purpose car	Delivery Van
Battery capacity [kWh]	42	80
Battery Roundtrip efficiency [%]	90%	
Dept of Discharge [%]	80%	
Battery derating factor [%/cycle]	0.00635 (hypothesis SOH = 80% @ 3500 cycles)	
EV max charging power [kW]	11	22
Charging station capacity [kW]	3.7	22
EV efficiency [kWh / 100km]	18.9 [19]	
Yearly distance covered [km] (approximate)	10,000 [20]	15,000 [20]

The main parameters influencing the simulation of EVs are battery capacity, maximum charging power, and efficiency (i.e. average electricity consumption per 100 km).

3. METHODOLOGY

The various case studies are compared from both an economic and energy perspective. Specifically, the following KPIs are evaluated:

- **Total annual energy shared by the REC:** as shared energy increases, revenues from incentives rise, thereby improving the benefits for users within the configuration.
- **Total annual incentive generated by the REC:** as the incentive grows, the benefits for users of the configuration increase accordingly.
- **Charging power (PC) of EVs:** charging power profiles of EVs are extracted, and average profiles are

determined for each typical day. Comparing these profiles across the different cases, it is possible to understand how charging power varies with the chosen charging strategy.

- **State of Charge (SOC) of EVs:** SOC profiles of EVs are extracted, and average profiles are determined for each typical day. Comparing these profiles across the different cases, allows an understanding of how SOC varies depending on the charging strategy. Furthermore, additional statistical insights can be obtained from box plots generated for each individual vehicle.

All these KPIs make it possible to evaluate how the economic benefits vary and to assess how users' "comfort" conditions change under different charging strategies.

To simulate the energy and economic flows of various users in the configuration and to model the operation of an Energy Community, the open-source Python library developed by RSE [21] was employed. The modelling of the EV charging with a "standard" strategy (*StC logic*) and with a "smart" strategy (*SC logic*) required the development of a dedicated simulation module; the corresponding implemented logic is described in the following sections. All the functions used to model EV charging profiles (with different control strategies), along with the related documentation, are available in the open-source repository [21]. The following paragraphs briefly introduce the key concepts underlying the methodology for simulating individual users' energy and economic flows, the REC simulation framework, and the methodology for simulating EV charging profiles with different control strategies. More detailed information is available in the documentation attached to the online repository.

4. Energy Community Simulator

Figure 1 shows the operating scheme of the REC simulator. While the electric vehicle model can be generalized, the energy shared and incentives calculations are tailored on the Italian context and regulatory framework, which play a relevant role in determining the EV smart charging control logics.

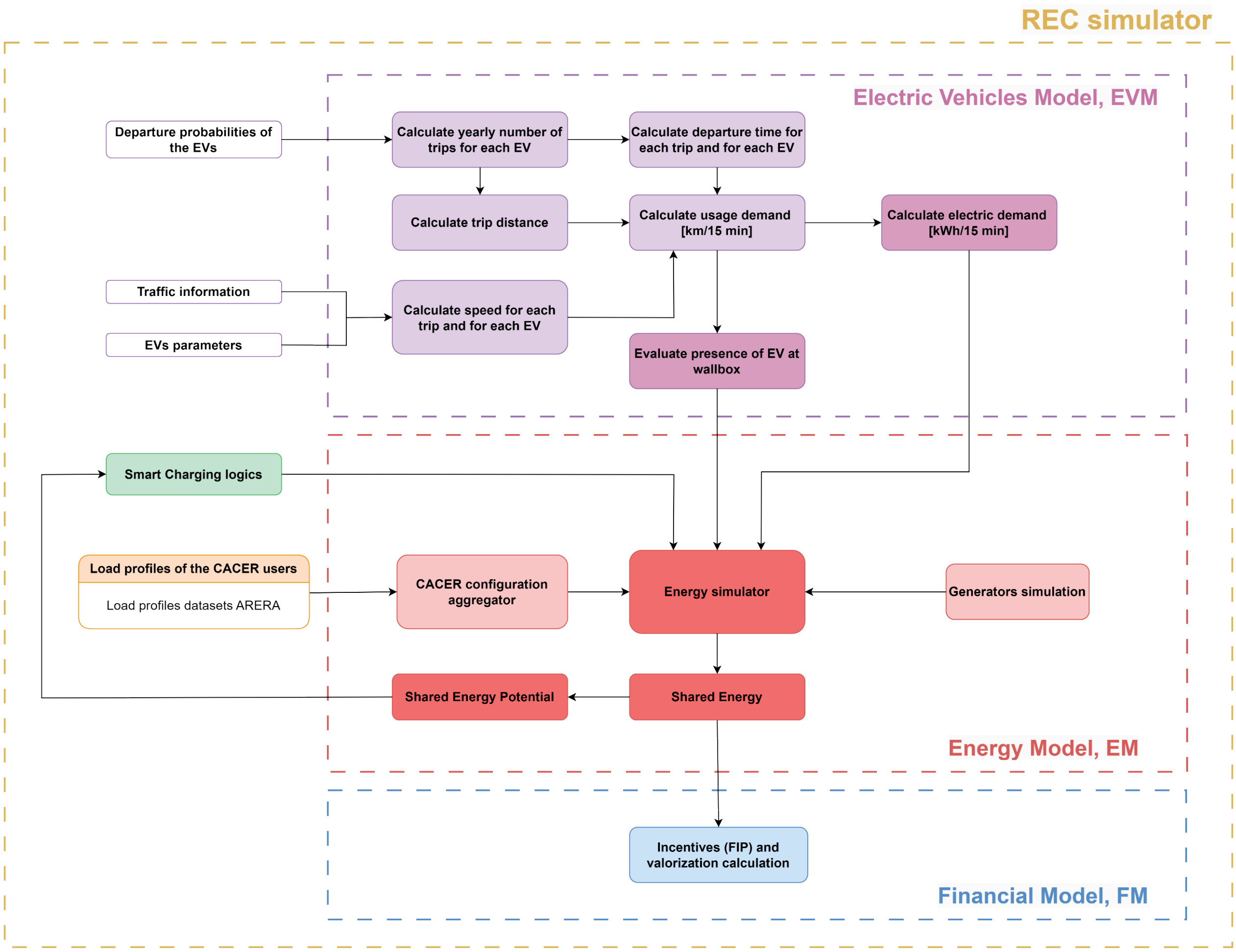

Fig. 1. Simulator workflow.

The simulator is composed of three different modules:

1. **Electric Vehicle Model (EVM)**, This module determines the consumption profiles of electric vehicles (kWh/15min) and their presence at the charging infrastructure. EV consumption profiles represent the vehicles' electricity use during different trips, while presence indicates whether the vehicle is connected to the charging station. To calculate these parameters, it is necessary to know the EV characteristics (particularly its efficiency), the traffic conditions affecting vehicle speed, the type of trip (local road,

connecting road, or arterial road), the number of annual trips, and the departure time of each individual trip. More detailed information on the electric vehicle simulation methodology is provided later.

2. **Energy Model (EM)** simulates the electricity consumption of each individual user (both domestic and commercial) as well as the production of photovoltaic systems. In addition, EM calculates the net exchange profiles with the electricity grid for each user. Specifically, at each timestep it evaluates:
   a. **Electricity consumption for charging EVs**, which depends on the state of charge of the vehicles when connected to the CS.
   b. **Energy consumed**, i.e., the energy consumed by the user for each instant of time, including the EVs consumption.
   c. **Energy produced**, i.e. the energy generated by production plants at each instant of time.
   d. **Direct Energy self-consumption**, i.e. the amount of energy produced by the generation plants that is immediately consumed by user loads.
   e. **Energy injected into the grid**, i.e. surplus energy produced that is not directly consumed by the user.
   f. **Energy drawn from the grid**, i.e. the energy consumed by the user net of direct self-consumption.

Shared energy, defined by Italian law as the minimum between the total withdrawn energy by users participating in the REC and the total injected energy by users participating in the REC on an hourly basis [5]. Shared energy is calculated using Equation 1.

$$shared\ energy\ (t) = \min\left(\sum_{i}^{N} withdrawn\ energy_{i,t}\,;\ \sum_{i}^{N} injected\ energy_{i,t}\right) \quad (1)$$

Here N represents the number of members of the REC (consuming and/or producing) and t represents the specific hour.

Shared Energy Potential, defined as the difference between the total energy injected by users participating in the REC and the total energy withdrawn by those users on an hourly basis. Only positive values are considered, while negative values are set to zero. This metric evaluates the REC's hourly potential for shared energy. It indicates the additional amount of user withdrawals required in each hour to maximize shared energy and, consequently, incentive revenues. In this study, higher consumption is achieved by adjusting the charging power of EVs. The "smart" charging strategy is described in more detail in the following sections. The shared energy potential is calculated using Equation 2.

$$shared\ energy\ potential(t) = max\left[\left(\sum_{k}^{M} injected\ energy_{k,t} - shared\ energy\ (t)\right); 0\right] \quad (2)$$

3. **Financial Model (FM):** these modules calculate the revenues obtained by participation in the REC. According to Italian legislation [5] an incentive is granted on the amount of energy shared within the configuration. Shared energy is calculated using Equation 1, while the corresponding incentive revenues are obtained through Equation 3, again calculated on an hourly basis.

$$yearly\ incentive\ revenues = \sum_{t=1}^{8760} FIP(t) \times energy\ shared\ (t) \quad (3)$$

Where is the hourly premium tariff, which depends on the power of the generation plants () and the hourly zonal price of electricity (). The hourly FIP is calculated using Equation 4.

$$FIP = \begin{cases} min[100; 60 + \max(0; 180 - ZP)] & if\ (P_{gen} > 600\ kW) \\ min[110; 70 + \max(0; 180 - ZP)] & if\ (200\ kW < P_{gen} < 600\ kW) \\ min[120; 80 + \max(0; 180 - ZP)] & if\ (P_{gen} \leq 200\ kW) \end{cases} \quad (4)$$

The FIP also includes a correction factor based on the location of the systems, which accounts for the different levels of solar radiation across Italian territory (providing additional financial support for region with lower irradiation levels).

In addition to the FIP, a bill tariff component is refunded, corresponding to the reduced network losses resulting from increased local self-consumption (*valorization*). This incentive is less significant than the FIP, but it is nevertheless calculated by the simulator. Further details on the calculation of this revenue component are provided in the *Integrated Text for Diffused Self-Consumption* [5].

5. Electric Vehicle Simulator

The module was developed from the perspective of the individual user's mobility demand, following a *bottom-up approach*. The algorithm is divided into two sections: the first defines the mobility demand of EVs and their presence at the charging station (purple section in Figure 1), while the second defines their charging strategy (green box in Figure 1). The first section of the algorithm therefore characterizes each individual trip of the different vehicles using a probabilistic approach, as described in the following steps:

1. The parameters of each vehicle, the characteristics of the charging infrastructure, and the usage habits of different user types (e.g. annual mileage, number of trips, etc.) are specified.
2. Daily probability distributions of vehicle movements are provided on a quarter-hourly basis and for typical days (workdays, Saturdays, and Sundays). In addition, weekly correction factors are applied to simulate different usage patterns across seasons. User-defined quarter-hourly departure probability profiles are then generated for the entire simulation period (1 year, 20 years, etc.), for each type of vehicle use (e.g., family use, commuting, commercial vehicle, heavy transport, forklift, etc.). Figure 2 shows the departure probability distributions for different day types and uses (Commercial EVs and Domestic EVs).
3. Depending on the specified type of use, an arbitrary value is assigned to the shape factor of the Weibull function, which defines the distribution of trip distances. This factor describes the shape of the distribution and affects both the standard deviation and the proximity of the mean value to zero. Based on the shape factor and the number of trips provided by the user, a function then calculates the scaling factor of the Weibull function to match the desired annual distance travelled (within a tolerance of a few hundred km).
4. Once these values are defined, a function iteratively simulates vehicle's movements, based on:
   a. **Departure time** derived from the probability of distribution of trip departures.
   b. **Distance** generated using the Weibull function.
   c. **Vehicle destinations** are defined as either a charging point (e.g., a wall box at home) or a generic destination without charging. Public charging stations are not considered in this study, as they are irrelevant to the current research.

Given the departure time and destination, each trip is divided into 15-minute intervals, considering the average vehicle speed according to the road type assumed for that segment (*Local* or "L", *Connection* or "C", *Arterial* or "A") and the estimated traffic conditions based on the time of day and day of the week. Table 4 summarizes the average speeds and distances travelled for the different road types.

Figure 3 shows the speed correction factors as a function of the time and type of day.

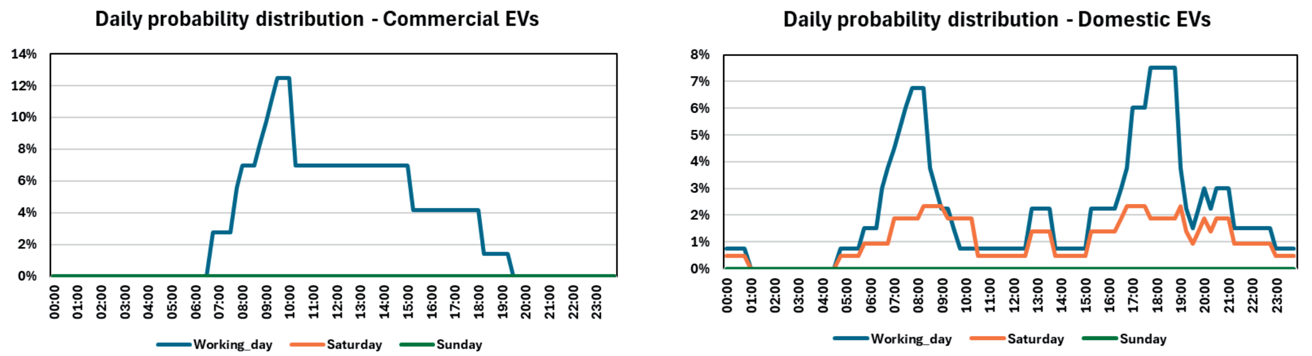

(a) **(b)**

Fig. 2. Probability of electric vehicle departure for different days of the week and for different vehicle types (commercial on the left and domestic on the right).

Table 4. Average travel speed and average distance traveled for different types of roads.

Functional Road Class	Section	Average speed [km/h]	Distance from departure/ arrival venue [km]
Local Roads	L	15	2
Connector Roads	C	30	5
Arterial Roads	A	100	n.a.

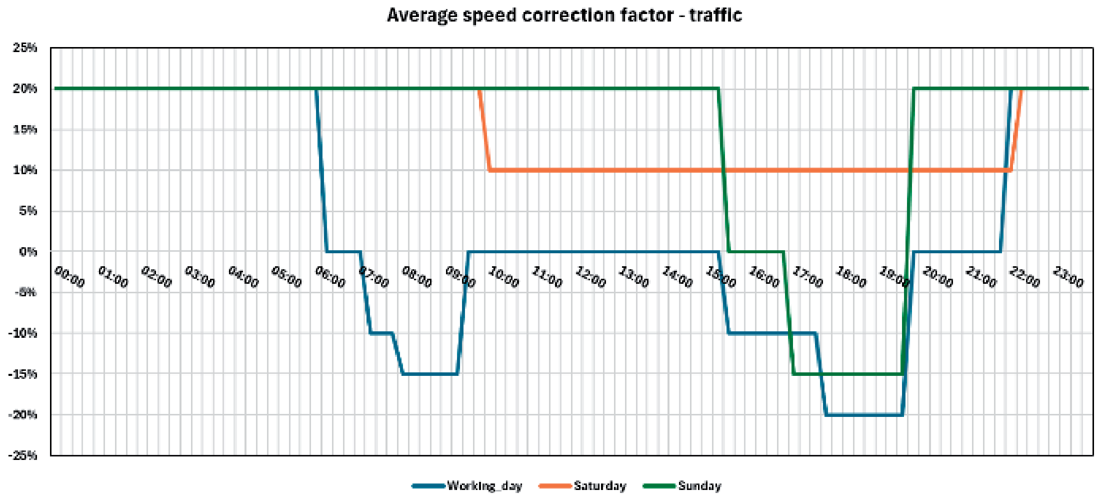

Fig. 3. Average speed correction factors due to traffic on different days of the week.

The average speed of the vehicle, the distance travelled, and the arrival time at the destination are then calculated. Once at its destination, the vehicle remains idle until the next trip. This procedure is repeated for each trip and each vehicle over the entire simulation horizon, resulting in a mobility demand matrix expressed in km per 15 min.

5. From the mobility demand matrix, the travel-related electricity consumption matrix is derived, converting km per 15 min into kWh per 15 min by applying an appropriate conversion factor. This factor may depend on the average speed at that moment, the outside temperature (and thus the season), and the characteristics of the individual vehicle (different make and model with varying performance). At present, a fixed conversion factor is applied.
6. For each trip, the vehicle's position relative to its reference charging point is tracked at each moment in time. A function determines whether the user, upon arriving at the charging point, connects the vehicle to the CS or not. This makes it possible to simulate different behaviors among users with varying charging habits, including those who may choose not to connect their EV to the CS.

This entire section of the algorithm is used to determine mobility demand (expressed in kWh per 15 minutes) and the presence of the electric vehicle at the CS.

At this point, as the energy demand for mobility is obtained, the EV charging and discharging algorithm steps in governing the battery energy flows. For each simulation timestep t, the model receives a theoretical energy flow at the battery terminals (positive if the charging power, negative if requested by the EV engine) and determines the actual battery behavior by considering charging/discharging efficiencies and SOC operational constraints. The model considers also losses for roundtrip efficiency, battery derating from aging effect. Starting from the SOC from the t-1 interval (here considered in kWh) and the theoretical energy flows at time t, the model computes the real flows by checking the battery constraints and applying the losses (gross and net are before and after applying the conversion efficiency). The model replicates the calculation iteratively. The model provides a computationally efficient representation suitable for large-scale energy simulations while neglecting voltage dynamics, thermal behavior, and power-dependent battery characteristics.

Describing the process with the equations, at each timestep, the theoretical energy exchanged at the battery terminals is partitioned into charging and discharging components:

$$E^{theor}_{charge,gross,t} = max\left(0;\ E^{theor}_{terminal,t}\right) \tag{5}$$

$$E^{theor}_{discharge,gross,t} = min\left(0;\ E^{theor}_{terminal,t}\right) \tag{6}$$

Conversion losses are represented through a half-cycle efficiency parameter, assumed identical for charge and discharge processes:

$$\varepsilon_{halfcycle} = \sqrt{\varepsilon_{roundtrip}} \tag{7}$$

where ε denotes the efficiency. The upper and lower charge boundaries (SOC, indicated in kWh) are computed based on the cycling historical information of the battery:

$$SOC_{max,t} = (1-d)^{N_t} * C \tag{8}$$

$$SOC_{min,t} = SOC_{max,t} * (1 - DoD) \tag{9}$$

where d is the battery derating factor to include loss of capacity due to aging (for single cycle, assumed constant during the battery lifetime), N the number of cycles at time t since commissioning, C is the battery rated capacity and DoD is the Dept od Discharge.

The SOC evolution is obtained by applying the corresponding efficiency-adjusted energy variation and enforcing minimum and maximum SOC constraints that represent the allowable operating range of the battery. Whenever the unconstrained SOC exceeds these limits, the stored energy is saturated accordingly:

$$\begin{cases} SOC_t = SOC_{\max,t};\ if\ SOC_{t-1} + E^{theor}_{halfcycle,t} > SOC_{max,t} \\ SOC_t = SOC_{min,t}\ ;if\ SOC_{t-1} + E^{theor}_{halfcycle,t} \le SOC_{min,t} \\ SOC_t = SOC_{t-1} + E^{theor}_{halfcycle,t};\ otherwise \end{cases} \tag{10}$$

$$SOC_{\%,t} = \frac{SOC_t}{SOC_{max,t}} \tag{11}$$

Conversion losses are represented through a half-cycle efficiency parameter, assumed identical for charge and discharge processes. The actual terminal energy exchange and the associated energy losses are subsequently recalculated from the constrained SOC variation, ensuring consistency between battery operation, efficiency effects, and capacity limitations:

$$E^{real}_{halfcycle,t} = SOC_t - SOC_{t-1} \tag{12}$$

$$E^{real}_{charge,net,t} = max\left(0;\ E^{real}_{halfcycle,t}\right) \tag{13}$$

$$E^{real}_{charge,gross,t} = \frac{E^{real}_{charge,net,t}}{\varepsilon_{halfcycle}} \tag{14}$$

$$E^{real}_{discharge,gross,t} = min\left(0;\ E^{real}_{halfcycle,t}\right) \tag{15}$$

$$E^{real}_{discharge,net,t} = E^{real}_{discharge,gross,t} * \varepsilon_{halfcycle} \tag{16}$$

$$E_{loss,t} = \left|E^{real}_{charge,net,t} - E^{real}_{charge,gross,t}\right| + \left|E^{real}_{discharge,gross,t} - E^{real}_{discharge,net,t}\right| \tag{17}$$

The outputs of the module are the updated SOC and the corrected charging/discharging energy flows at the terminals for timestep t.

At this stage, the EVs charging strategy can be defined, which determines the user's electricity consumption due to charging. Two charging strategies are modelled:

- **Standard charging strategy (StC logic)**, in this case EVs, once connected to the CS, are charged at the maximum available charging power. This maximum charging power depends on the contractual power of the delivery point, the user's concurrent consumption, the maximum power deliverable by the CS and the EV maximum charging power. The maximum charging power is calculated using Equation 18.

$$P_{C,max}(t) = min\left[\left(P_{POD} - \sum_i P_{load,i}(t)\right);\ P_{CS,max};P_{EV,max}\right] \tag{18}$$

Where is the contractual power of the delivery point, reported in Table 1, is the power of the i-th load at time , is the maximum charging power of the CS, and is the maximum charging power of the electric vehicle. It was assumed that the commercial user's EV charging point includes a contractual power limiter, even though Italian legislation allows the installation of delivery points without a limiter and thus without any contractual power restriction.

- **"Smart" charging strategy (SC logic)**, This charging strategy is applied to both Commercial and Domestic EVs). Charging is prevented if no shared energy potential is available, and it can be partially limited or even suspended when necessary. Charging power is modulated by adjusting the variation ranges as the SOC changes. Specifically, a minimum charging power () and a maximum charging power () are defined as a function of the EV's SOC (Figure 4). The charging measurement, management, and control system checks whether shared energy potential is available in the configuration and adjusts charging power accordingly within the power ranges described below. On working days (except for Friday, Figure 4a), vehicles always charge at maximum power up to a SOC equal to . Between and of the SOC, partial power can be achieved up to of . Beyond , charging can be further reduced without limits, even to the point of cancellation. On Fridays (Figure 4b), vehicles charge at the maximum power when SOC is less than , while SOC values above charging can be reduced to , since rapid completion of charging is not required. On Saturdays and Sundays (Figures 4c and 4d respectively), charging power ranges are wider, allowing for greater flexibility. After Sunday midnight, however, a stricter limit is reinstated as the weekday strategy applies again. The SOC threshold ensures a minimum level of charge, reducing the risk of EVs not having sufficient energy for travel. The specific different distribution adopted for Fridays was designed to avoid full charging and to preserve flexibility that can be exploited during the weekend, when EVs are generally unused. Summarizing, part of the charging is prioritized for workdays and during the production period of the generation plants.

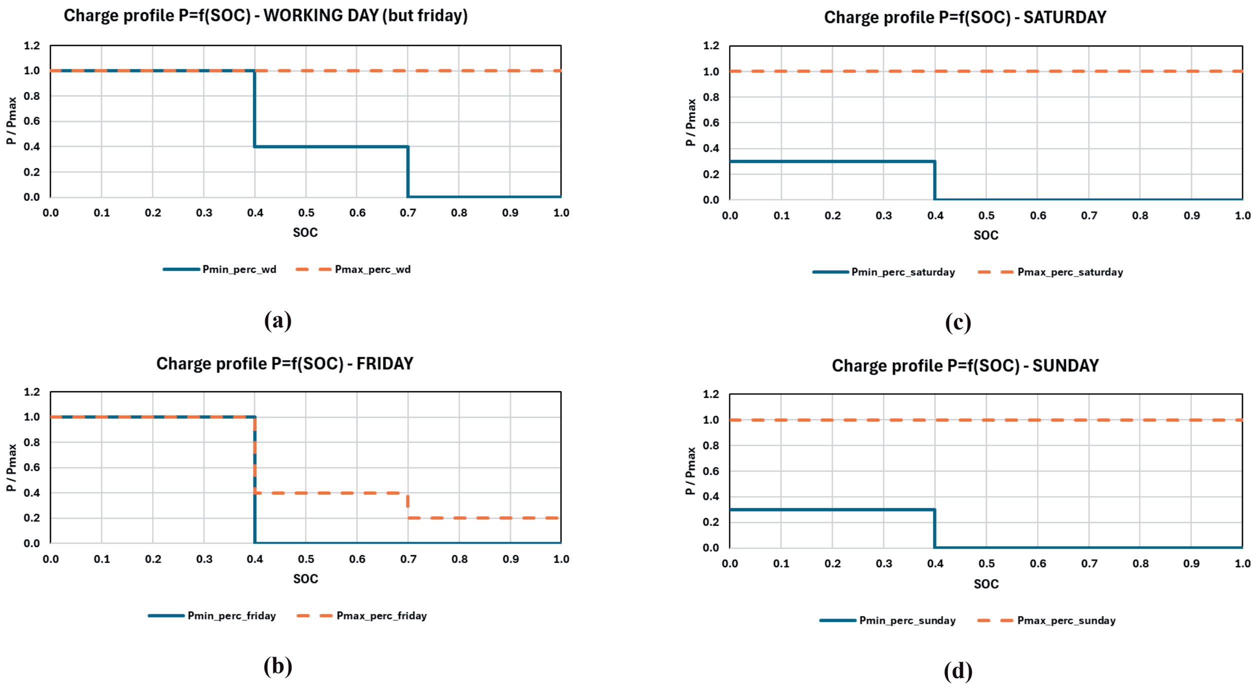

Fig. 4. Minimum and maximum power limits (nominal values compared to the maximum charging power Pmax) as function of SOC, for different days of the week: (a) - Working day but Friday; (b) - Friday; (c) - Saturday; (d) - Sunday.

At each timestep t, the shared energy potential is calculated and allocated among the EVs according to their availability (Figure 5). Specifically, the shared energy potential is divided into equal portions for all available vehicles, so the controller makes the power injection request and checks whether each vehicle can absorb it. In the example shown in Figure 5, during the iteration *n*, vehicle EV4 cannot retrieve the allocated share and is therefore excluded from the calculation, while vehicle EV3 can only partially. This energy that is left out becomes the input of the second iteration and thus redistributed into equal shares between updated list of vehicles EV1 and EV2 (as EV3 and EV4 are no longer available). The power allocation request is again checked at vehicles level, and it is found that vehicle EV2 can only partially absorb it (iteration). Finally, the remaining excess is absorbed by vehicle EV1, which still had available capacity in this example (iteration). At certain timesteps, it may also happen that the vehicles do not have sufficient availability to meet the controller's requests, meaning that not all the potential is converted into shared energy. The availability of EVs depends on the vehicle's SOC, infrastructure constraints and the power available at the point of delivery at given time, given by the difference between the contracted power and the user's current electricity consumption ().

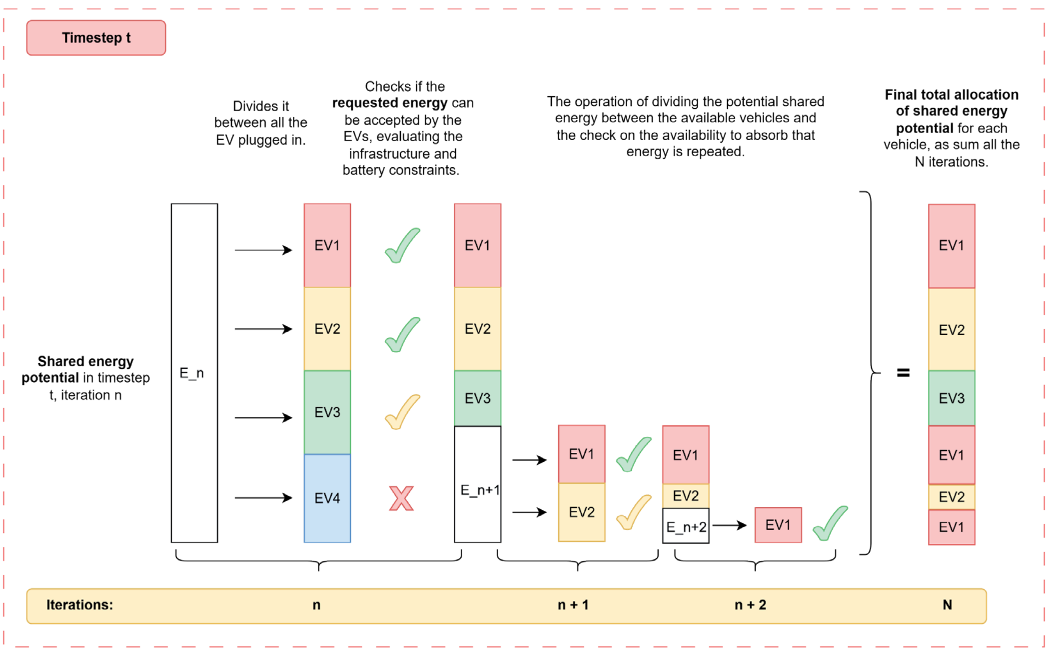

Fig. 5. Logic for allocating shared energy potential to different EVs (example for 4 EVs).

6. RESULTS

Figure 6 shows the average charging powers of the different EVs on various types of days (working day, Friday, Saturday, and Sunday), under different charging strategies (6-a for *StC logic* and 6-b for *SC logic*).

As expected, *SC logic* shifts EV charging from nighttime to daytime, thereby increasing the energy shared within the community. In the SC case, charging is significantly reduced since it only occurs when the SOC falls below the thresholds of 40% or 70%, as described in Figure 4.

Simulation results indicate that under *StC logic*, vehicles generally reach full charge by Friday night. Consequently, little charging is required over the weekend, except for domestic users who use their cars on Saturday, while commercial vehicles remain parked. Using the *SC logic*, EVs do not fully recover SOC during workdays due to power limitations, but they compensate over the weekend, when abundant solar energy is available and industrial loads are low.

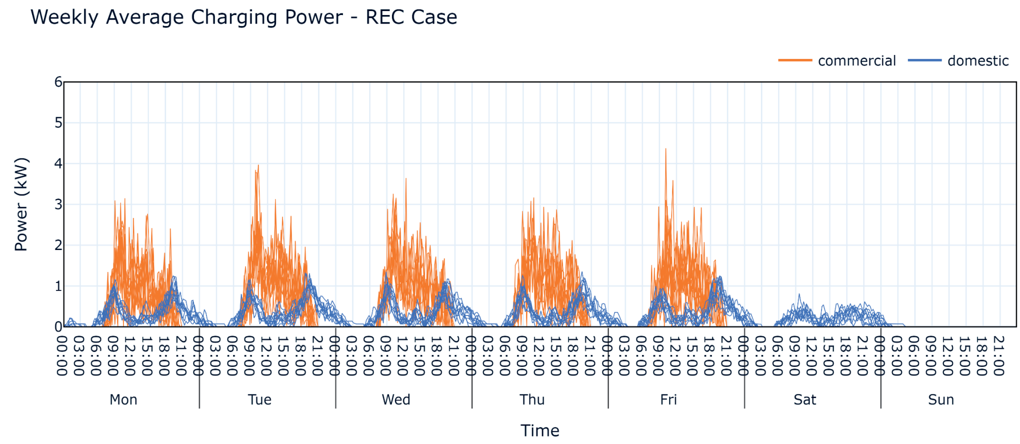

(a)

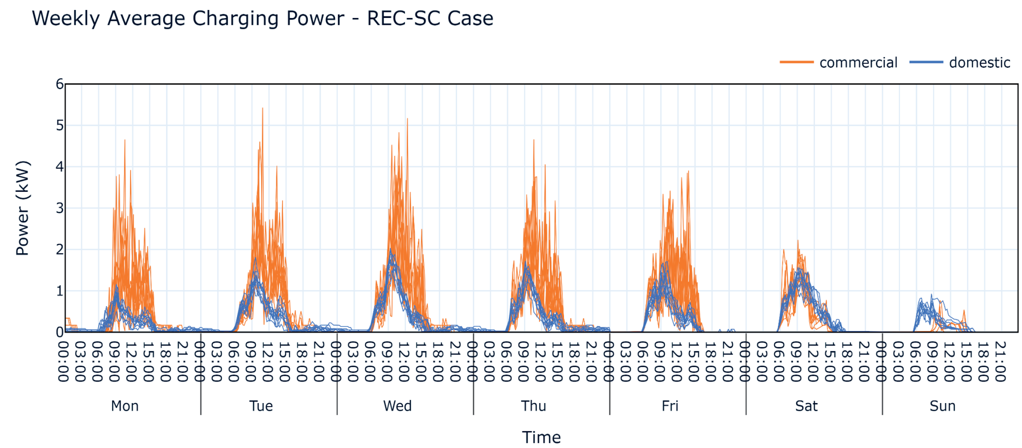

(b)

Fig. 6. Average weekly charging power profiles for all EVs (domestic in blue and commercial in orange) on different days of the week, for (6a) StC logic and (6b) for SC logic**.**

Figure 7 shows the average weekly SOC using *StC* (Figure 7-a) and *SC logics* (Figure 7-b). In general, SOC levels are lower in the *SC case*, reaching a minimum between Friday and Saturday, while remains relatively high and stable in the *StC case*. As expected, the SOC patterns reflect the combination of mobility demand (SOC decreases when EV is in use), charging events described above (SOC increases when EV is plugged and charging), and idle conditions when the vehicle is parked but not charging (SOC remains stable, typically at night, in the early morning, or during weekends).

By adopting *SC logic*, SOC becomes more stable during evening and nighttime hours, as consequence of the controller's charging limitations. Conversely in the SC case, SOC increases in the morning as solar irradiance and PV production rise and then stabilizes when users begin driving their vehicles.

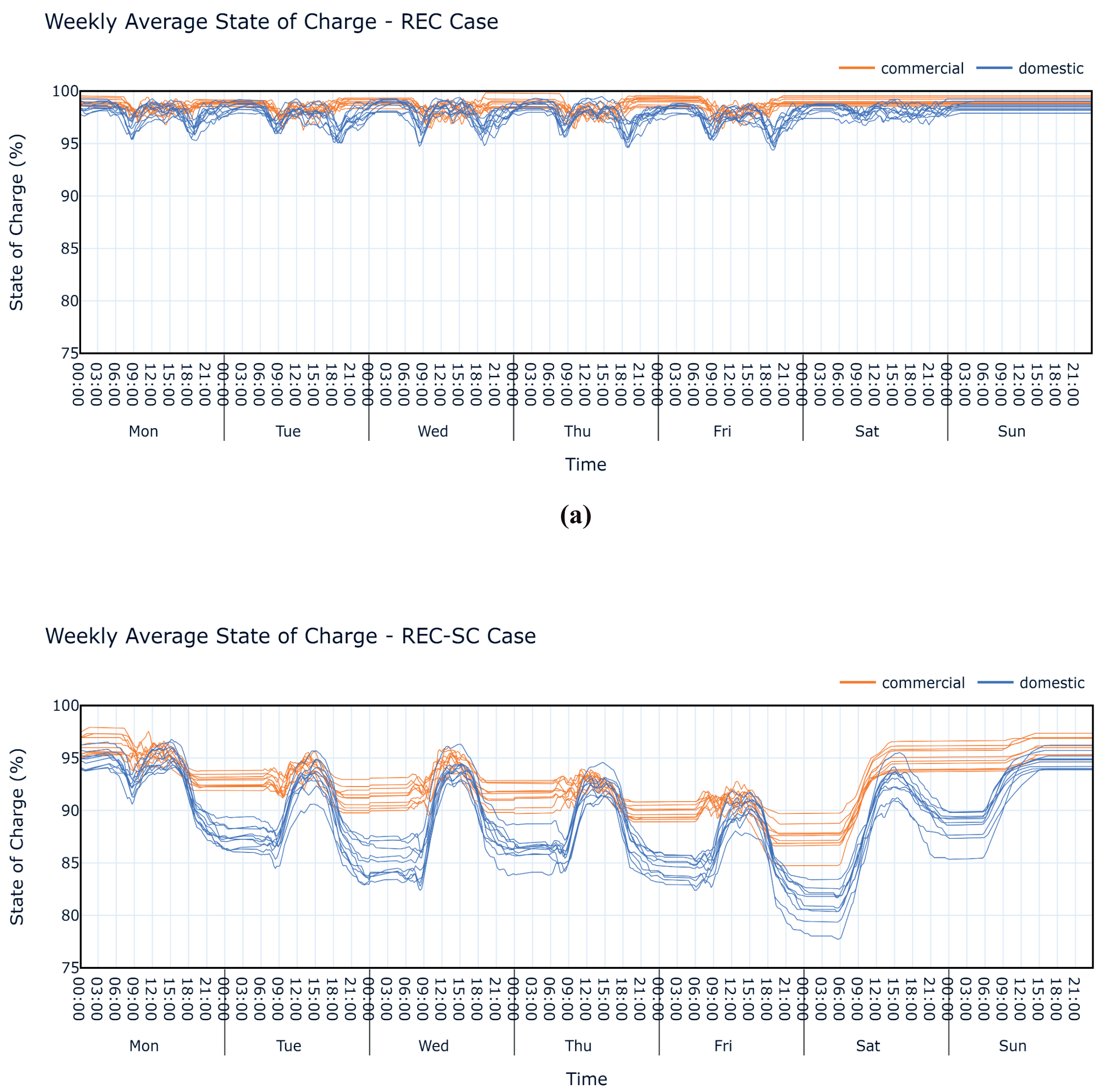

(a)

(b)

Fig. 7. Average SOC profiles for different EVs (domestic in blue and commercial in orange) on different days of the week, for (7a) StC logic and (7b) SC logic.

As shown in the previous graphs, the average SOC of EVs decreases when *SC logic* is applied. This trend is also evident in the boxplots shown in Figure 8, which illustrates the SOC distributions for different vehicles. Using the *StC logic* (REC and reference cases), SOC values are generally very high, with the 5th percentile typically above . In contrast, using *SC logic* (REC – SC case), SOC values are considerably lower, with the 5th percentile around for commercial EVs and for domestic EVs. This occurs because *SC logic* imposes several charging limitations based on PV production and real-time SOC, forcing EVs to wait for optimal charging conditions. Regarding the lowest recorded values, represented by outliers (dots), they never fall below . This means that vehicles always maintain a state of charge sufficient to meet user's mobility needs. Using the *SC logic*, however, SOC values exhibit a wider distribution, highlighting the variability introduced by this charging strategy. Even in this case, SOC levels generally remain high, although outliers may drop to low value without ever reaching zero. Consequently, the "smart" charging strategy reduces user comfort but does not cause service disruptions. It is worth noting that the SOC levels are determined by the charging power constraints imposed according to the SOC thresholds (40% and 70%) illustrated in Figure 4. An increase in these thresholds would lead to higher allowable charging power and, consequently, higher SOC levels; however, this would occur at the expense of reduced charging flexibility, thereby diminishing the potential for additional incentives.

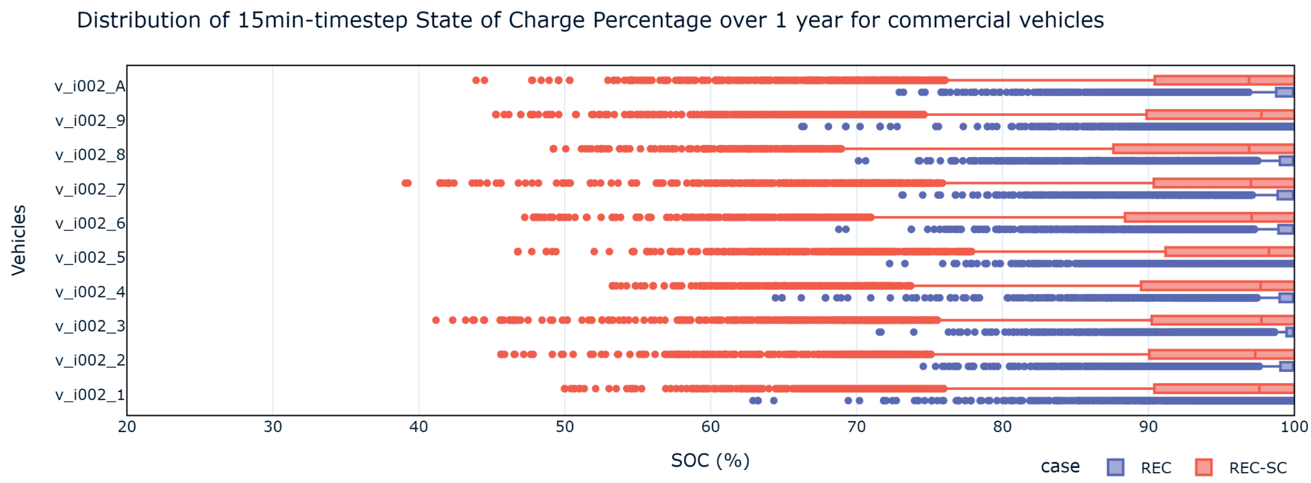

(a)

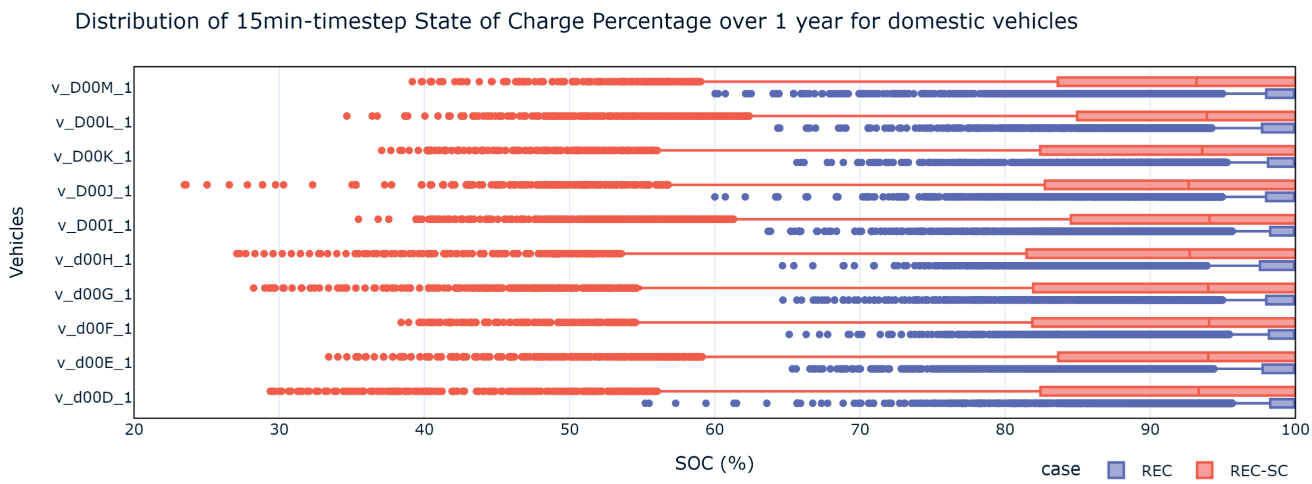

(b)

Fig. 8. Boxplot of the SOC for different EVs - commercial EVs in Figure 8-a and domestic EVs in Figure 8-b - using StC logic (REC case) and SC logic (REC-SC case).

To investigate a real behavior rather than averaged values, Figure 9 shows the energy flows results for the REC and REC-SC scenarios during a specific week in March. Non-shiftable REC base load is shown in yellow (household and commercial user consumption), while EV charging is highlighted in blue. In the REC scenario, charging is distributed between day and night and depends solely on the vehicles' SOC and their presence at the charging station.

In the REC-SC scenario, however, the "smart" charging strategy concentrates charging during PV system production hours (the production curve is represented by the red line). Moreover, on days with low PV generation and insufficient shared energy potential (as on Monday in the figure), vehicles charge only to meet minimum SOC requirements (hence the small blue lines on Monday and Tuesday evenings in Figure 9-b).

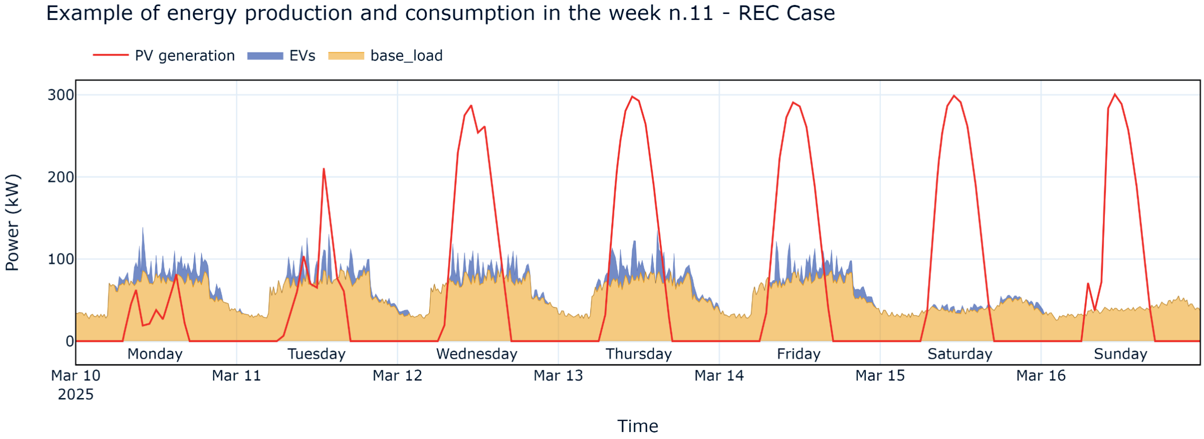

(a)

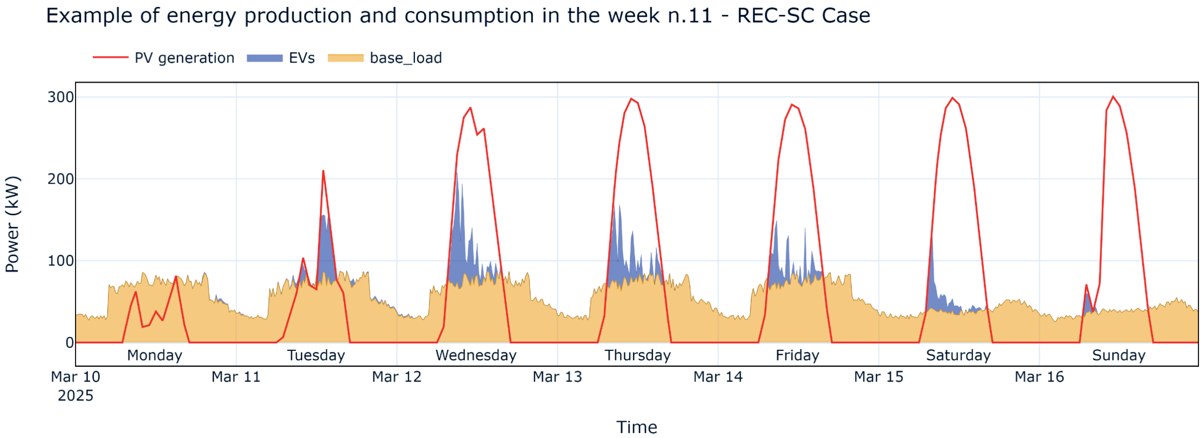

(b)

Fig. 9. Aggregate production profiles of photovoltaic systems (red line), aggregate base load of the configuration (yellow area), and aggregate load of EVs (blue area) for a specific week under consideration. Figure 9-a uses StC logic and Figure 9-b uses SC logic.

To conclude, Table 5 reports the results for the REC's annual shared energy and the annual incentive-related revenues obtained in the different case studies. Aggregating all users within a REC generates approximately thousand in incentives, without requiring any changes in energy generation and consumption (including EV charging) compared to the reference case.

Moreover, adopting a smart charging system increases shared energy by , raising incentive revenues to thousand (), all without causing any disruptions to users' mobility services. These results highlight the relevant benefits that can be achieved by participating in an energy community and by additionally adopting the "smart" charging strategy proposed in this study.

Table 5. Annual shared energy and annual incentive revenues in different cases.

Case study	Yearly Shared Energy [MWh]	Yearly Incentive Revenues [€]
Ref case	n.a.	n.a.
REC case	56.3	€ 5,684.86
REC – SC case	82.8	€ 8,527.83

When results are normalized to the average vehicle of the REC fleet, each smartly controlled generates an additional of shared energy and in incentives per year, with the potential to be maintained over a 20-year period.

7. CONCLUSIONS

The simulations and output data show that the REC can leverage these storage resources to generate approximately 47% increase in energy sharing and 50% additional incentives, by adopting a centralized smart charging for the 20 EV without disruptions in services. In other words, EV users do not experience any shortage of charge availability for their mobility needs over the 1-year simulation. Although the smart charging strategy leads to greater variability in the state of charge during the week, no vehicle ever suffers from insufficient charge. This was demonstrated by investigating the 15-min SOC distributions, which show that none of the EVs' bottom outliers ever reach critical states. The smart charging logic proposed in this study has the advantage of avoiding the need to forecast the configuration's consumption and production data. Specifically, EV charging power is regulated based on the shared energy potential of the Energy Community, while maximum and minimum charging limits are defined as function of the EVs state of charge. Naturally, implementing this charging strategy in a real-world context requires investment in measurement, control, and management systems for both EVs and the Energy Community, which architecture and costs were not the scope of this study. Furthermore, EV charging load shifting was demonstrated to increase local self-consumption, with simulations reporting still high SOCs which may leave room for other applications, such as V2G or other flexibility purposes. In conclusion, smart load shifting in electric mobility applications can generate relevant additional value to energy communities with relatively simple optimization solutions.

8. Nomenclature

Parameter notation	Parameter definition	Unit
REC	Renewable Energy Community	-
EV	Electric Vehicle	-
CEV	Commercial Electric Vehicle (EVs of the commercial user)	-
DEV	Domestic Electric Vehicle	-
CS	Charging Station	-
FIP	Premium Feed-in	€/kWh
ZP	Zonal Price	€/kWh
	Installed capacity of the generators	kW
SOC	State of Charge	%
	Maximum charging power (Equation 3)	kW
	Contractual power	kW
	Power absorbed by the load	kW
	Maximum charging power of the Charging Station	kW
	Maximum charging power of the Electric Vehicle	kW
	Minimum charging power of the Electric Vehicle	kW

References

[1] European Parliament and Council, "DIRECTIVE (EU) 2018/2001 OF THE EUROPEAN PARLIAMENT AND OF THE COUNCIL," [Online]. Available: https://eur-lex.europa.eu/eli/dir/2018/2001/oj/eng. [Accessed 09 2025].

[2] European Parliament and Council, "DIRECTIVE (EU) 2019/94," [Online]. Available: https://eur-lex.europa.eu/legal-content/IT/ALL/?uri=CELEX%3A32019L0944. [Accessed 09 2025].

[3] *Decreto Legge 30 dicembre 2019, n. 162,* Rome: Gazzetta Ufficiale, 2019.

[4] "DECRETO LEGISLATIVO 8 novembre 2021, n. 199," 8 11 2021. [Online]. Available: https://www.gazzettaufficiale.it/eli/id/2021/11/30/21G00214/sg. [Accessed 09 2025].

[5] Autorità di Regolazione per Energia Reti e Ambiente (ARERA), "Testo Integrato Autoconsumo Diffuso," [Online]. Available: https://www.arera.it/fileadmin/allegati/docs/22/727-22TIAD.pdf. [Accessed 09 2025].

[6] Ministero dell'Ambiente e della Sicurezza Energetica, Decreto MASE n. 414 del 07/12/2023, Rome: Ministero dell'Ambiente e della Sicurezza Energetica, 2023.

[7] Gestore Servizi Energetici, GSE, "gse.it," [Online]. Available: https://www.gse.it/documenti_site/Documenti%20GSE/Servizi%20per%20te/AUTOCONSUMO/Gruppi%20di%20autoconsumatori%20e%20comunita%20di%20energia%20rinnovabile/Regole%20e%20procedure/ALLEGATO%201%20Regole%20O. [Accessed 09 2025].

[8] A.-M. Borbely and J. F. Kreider, Distributed Generation: The Power Paradigm for the New Millennium, CRC Press, 2001.

[9] A. Pronti and R. Zoboli, "Something new under the sun. A spatial econometric analysis of the adoption of photovoltaic systems in Italy," *Energy Economics,* vol. 134, 2024.

[10] P. Denholm, M. O'Connell, G. Brinkman and J. Jorgenson, "Overgeneration from Solar Energy in California: A Field Guide to the Duck Chart," National Renewable Energy Laboratory - NREL, 2015.

[11] S. Borlase, Smart Grids: Infrastructure, Technology, and Solutions, CRC Press, 2016.

[12] A. Rollo, P. Serafini, F. Aleotti, D. Cilio, E. Morandini, D. Moneta, M. Rossi, M. Zulianello and V. Angelucci, "Load Shifting and Demand-Side Management in Renewable Energy Communities: Simulations of Different Technological Configurations," *Energies,* 2025.

[13] A. Karameros, A. Chassiakos and S. Kararzas, "Design and Evaluation of a Micro-Grid Energy Management Scheme Focusing on the Integration of Electric Vehicles," *Journal of Sustainable Development of Energy, Water and Environment Systems,* vol. 11, no. 1, 2023.

[14] P. Moura, G. K. Yu and J. Mohammadi, "Management of Electric Vehicles as Flexibility Resource for Optimized Integration of Renewable Energy with Large Buildings," in *2020 IEEE PES Innovative Smart Grid Technologies Europe (ISGT-Europe)*, The Hague, 2020.

[15] P. Marcolin, S. Salamone, A. Cazzaniga and G. Mauri, "EV Smart Charging strategies for reduced operating costs and grid impact: A case study on a workplace charging infrastructure," *Accepted for pubblication in CIRED 2025 - 28th International Conference and Exhibition on Electricity Distribution,* 2025.

[16] S. J. Shern, M. T. Sarker, G. Ramasamy, S. P. Thiagarajah, F. A. Farid and S. T. Suganthi, *Artificial Intelligence-Based Electric Vehicle Smart Charging System in Malaysia,* MDPI on behalf of the World Electric Vehicle Association, 2024.

[17] X. Wang and Y. Chen, *Carbon-Aware Quantification of Real-Time Aggregate Power Flexibility of Electric Vehicles,* IEEE Transactions on Smart Grid, 2024.

[18] P. Bastida-Molina, Y. Rivera, C. Berna-Escriche, D. Blanco and L. Álvarez-Piñeiro, "Challenges and Opportunities in Electric Vehicle Charging: Harnessing Solar Photovoltaic Surpluses for Demand-Side Management," *Machines,* 2024.

[19] Fully Charged, "ev-database.org," [Online]. Available: https://ev-database.org/cheatsheet/energy-consumption-electric-car. [Accessed 09 2025].

[20] ISTAT, "LE PERCORRENZE DEI VEICOLI STRADALI CIRCOLANTI," 2021. [Online]. Available: https://www.istat.it/wp-content/uploads/2025/06/Le-percorrenze-dei-veicoli-stradali-circolanti.pdf. [Accessed 05 06 2025].

[21] Github - RSE, "github.com," [Online]. Available: https://github.com/RSE-EUT/CACER-simulator. [Accessed 09 2025].

Kledi Xhaxhiu[1,2], Avni Berisha[2,3], Nensi Isak[1,2] , Besnik Baraj[1], Bujar Seiti[1]*

Toward a comprehensive remediation of polluted waters using a compact composite layered material

[1]Department of Chemistry, Faculty of Natural Sciences, University of Tirana, Blv. Zogu I, No. 25/1, 1001 Tirana, Albania
[2]Regional Centre of Nanotechnology (NANOBALKAN), Academy of Sciences of Albania, Murat Toptani, Av., 1000 Tirana, Albania
[3]Department of Chemistry, Faculty of Natural and Mathematics Science, University of Prishtina, 10000 Prishtina, Kosovo
*Corresponding author: kledi.xhaxhiu@fshn.edu.al

Original scientific paper
Received: January 7, 2026
Accepted: March 8, 2026
https://doi.org/10.65776/ep.21.1.3

Abstract

This study proposes and conceptally develops a compact composite layered material for simultaneous removal of organic pollutants and heavy metals from contaminated waters. The objective is the evaluation of the adsorption performance of natural and modified clay minerals toward selected pesticides (atrazine, chlorpyrifos, glyphosate) and pharmaceuticals (azithromycin, paracetamol, ibuprofen), and to assess the heavy-metal uptake capacity of layered manganese oxides (birnessites and buserites), with the aim of integrating them into a multifunctional composite adsorbent. The methodology combines previously obtained experimental results on Albanian natural and activated clays and synthetic manganese oxides with an extensive quantitative literature analysis. Adsorption capacities were compared, and mechanisms were interpreted using well-known isotherm models.

Natural clays exhibit adsorption capacities up to 200 mg/g for atrazine, 150 mg/g for chlorpyrifos, 130 mg/g for glyphosate, 150 mg/g for azithromycin, 200 mg/g for paracetamol, and 100 mg/g for ibuprofen. After activation, capacities increased by approximately 40–60%, exceeding 300 mg/g for selected compounds. Layered manganese oxides demonstrated heavy-metal adsorption up to 400 mg/g in natural forms and above 600 mg/g in synthetic variants, particularly for Pb^{2+} *and* Hg^{2+}*. Based on these findings, a compact clay - birnessite/buserite composite is proposed as a universal adsorbent capable of addressing complex pollutant mixtures. Preliminary energy and sustainability analysis indicates that thermal regeneration requires approximately 150-200 kWh per ton of exhausted composite, which could be feasibly supplied by a small wind turbine of 10 kW capacity running at 30% capacity or small-scale solar installations. The proposed material offers a scalable, low-cost and environmentally compatible solution for integrated water remediation.*

Keywords*: Clays, birnessites/buserites, composite material, pollutants, water remediation*

1. Introduction

Water pollution constitutes one of the most pressing environmental and societal challenges worldwide, exacerbated by industrial growth, intensive agricultural practices, urbanization, and climate-change-driven water scarcity [1, 2]. Surface waters and groundwater resources are increasingly contaminated by complex mixtures of organic and inorganic pollutants, among which pesticides, pharmaceuticals, dyes, and heavy metals are particularly problematic due to their persistence, toxicity, and potential for bioaccumulation [3, 4]. Pesticides remain indispensable in modern agriculture, yet their extensive and often uncontrolled application has resulted in widespread contamination of soils and water bodies. Compounds such as atrazine, glyphosate, chlorpyrifos, metribuzin, methomyl, diuron, carbaryl, and alachlor are frequently detected in surface waters and aquifers. Their presence is often at locations distant from their application sites due to leaching, runoff, and atmospheric transport [5, 6, 7]. This widespread distribution poses significant risks to aquatic ecosystems and human health, including endocrine disruption, neurotoxicity, and carcinogenic effects. Similarly, pharmaceutical compounds have become ubiquitous environmental contaminants due to their extensive use and incomplete removal in conventional wastewater treatment plants. Substances such as the antibiotic azithromycin and the common analgesics paracetamol and ibuprofen are frequently detected in aquatic systems, raising concerns about antibiotic resistance and chronic ecological effects. Adsorption onto clay minerals has emerged as a promising mechanism for the removal of these pharmaceuticals from water, leveraging the charged surfaces and modifiable interlayer spaces of clays to capture a variety of organic molecules [8, 9, 10, 11, 12].

Conventional water treatment technologies like coagulation, flocculation, membrane filtration, and advanced oxidation processes are often inadequate or economically prohibitive for the removal of such micropollutants, particularly when present at low concentrations and in complex mixtures [13, 14]. In this context, adsorption-based remediation has emerged as a technically simple, cost-effective, and scalable alternative, capable of addressing a wide range of contaminants simultaneously [15].

Clay minerals represent one of the most extensively studied classes of natural adsorbents for organic pollutant removal. Their abundance, low cost, high specific surface area, and permanent negative charge make them particularly attractive for environmental applications [16]. Numerous studies have demonstrated the ability of natural and modified clays to adsorb pesticides and pharmaceuticals through mechanisms such as cation exchange, hydrogen bonding, and hydrophobic interactions [5, 6, 17]. Recent reviews focusing on diuron, carbaryl, and alachlor adsorption have highlighted the critical role of clay type, surface modification, and solution chemistry in controlling adsorption efficiency [7]. Parallel to organic contamination, heavy metal pollution represents another major threat to water quality.

Metals such as Pb^{2+}, Cd^{2+}, Cu^{2+}, Zn^{2+}, and Hg^{2+} originate from industrial discharges, mining activities, and natural geochemical processes. Unlike organic pollutants, heavy metals are non-degradable and require immobilization or removal from the aqueous phase [18, 19]. Layered manganese oxides, particularly birnessite and its hydrated analogue buserite, have been identified as highly efficient adsorbents for heavy metals due to their ion-exchange capacity, redox activity, and structural flexibility [20, 21]. Previous research conducted by us and collaborators has demonstrated the effectiveness of Albanian natural and activated clays for the removal of metribuzin and methomyl from contaminated waters [22, 23, 24]. Complementary studies have shown that synthetic birnessites and buserites act as powerful traps for heavy metal cations, with adsorption capacities exceeding those of many conventional adsorbents [25].

Beyond these broad pollutant classes, this study specifically sheds light on the role of natural and modified clay minerals in adsorbing both widely used pesticides, such as atrazine, chlorpyrifos, and glyphosate, and a group of emerging pharmaceutical contaminants, including azithromycin, paracetamol, and ibuprofen. The co-occurrence of these substances in water bodies necessitates remediation strategies capable of addressing such diverse chemical groups simultaneously. This underpins the relevance of investigating clay-based adsorbents for this combined purpose. As a follow up of these findings and based on the extensive literature concerning pesticide adsorption on clays and metal uptake by manganese oxides, the present paper aims to propose and conceptually develop a compact composite layered material combining clays with birnessites/buserites. Such a composite is designed to function as a universal adsorbent, capable of simultaneously removing organic pollutants and heavy metals from polluted waters. This study integrates experimental insights from previous studies with enriched discussion based on recent literature, particularly focusing on pesticide, pharmaceutical-clay interactions, heavy metal-layered manganese oxides adsorption mechanisms, and environmental remediation strategies.

2. Study methodology

The present work is based on a synthesis of experimental data obtained in earlier investigations carried by us, complemented by an in-depth analysis of recent literature on adsorption-based water remediation. Particular attention was given to studies addressing the adsorption of pesticides (including atrazine, chlorpyrifos, glyphosate, azithromycin, paracetamol and ibuprofen) on natural and modified clays, as well as the uptake of heavy metal cations by layered manganese oxides such as birnessites and buserites.

The data presented in Figures 2, 3, and 5 were compiled from a comprehensive review of peer-reviewed literature. For figures 2 and 3, the adsorption capacities (mg/g) for each pollutant-clay combination were extracted from studies reporting equilibrium batch adsorption experiments. literature-reported values and experimental adsorption data obtained under the following representative laboratory conditions: Initial pollutant concentration: 50–200 mg/L, adsorbent dosage: 0.5–2 g/L, pH range: 5–7 for pesticides and pharmaceuticals, contact time: 24 h equilibrium, temperature: 298 ± 2 K, agitation speed: 150 rpm. The adsorption capacity (q_e) was calculated using the equation (1)

$$q_e = \frac{(C_0 - C_e)V}{m}$$

where C_0 and Ce are initial and equilibrium concentrations (mg/L), V is solution volume (L), and m is adsorbent mass (g).

Heavy-metal adsorption data presented in Figure 5 were obtained from both prior experimental work and literature under comparable equilibrium conditions, typically within pH 5–6 to prevent metal precipitation. Isotherm fitting was performed using Langmuir and Freundlich models. The values represent maximum adsorption capacities derived from Langmuir isotherm model fits. Where multiple values existed for a similar clay-pollutant pair, a representative range or maximum value was selected to illustrate the potential of the material.

Natural Albanian clays, previously characterized by X-ray diffraction, scanning electron microscopy, and chemical analysis, served as representative clay materials. Activation procedures reported in the literature include acid treatment, thermal activation, and cation exchange, all aimed at enhancing surface area, porosity, and adsorption capacity [26]. Birnessites and buserites were considered in both natural and synthetic forms, with emphasis on sodium-exchanged and hydrated variants known for their high ion-exchange capacity [20, 25]. Adsorption data reported in the literature were analyzed in terms of equilibrium capacities, kinetics, and controlling mechanisms. Where applicable, adsorption behavior was interpreted using classical isotherm models such as Langmuir and Freundlich, which remain widely employed for describing pollutant uptake on heterogeneous surfaces [27, 28].

3. Clays in organic pollutant removal

Clays are natural minerals made of thin layers. These layers consist of tetrahedral silica and octahedral alumina or magnesia sheets, stacked together and held by cations like sodium or calcium [16, 29]. This structure creates spaces between the layers that can expand to store water or capture pollutant molecules (**Fig. 1**). The most effective clays for adsorption have a 2:1 layer structure, which allows them to swell and host various molecules [5, 16]. These interlayer spaces and surfaces act as active sites where organic pollutants can be trapped. Pesticides, pharmaceuticals, and dyes can attach to clay surfaces through different forces, such as cation exchange, hydrogen bonding, or van der Waals interactions [5, 30]. The natural negative charge of clays attracts positively charged organic molecules. Furthermore, clays can be modified with surfactants or acid to improve their ability to capture neutral or hydrophobic pollutants [14, 26].

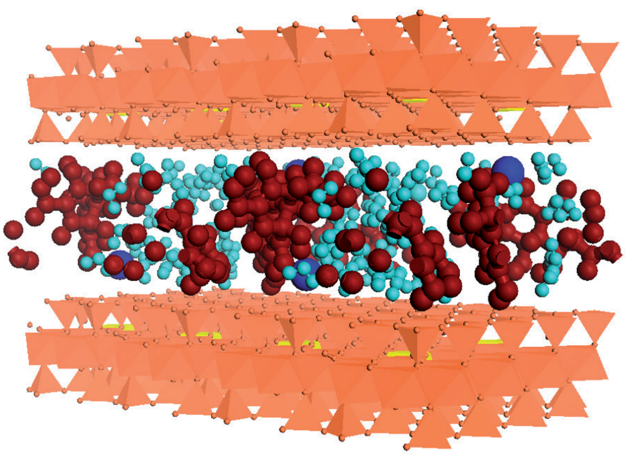

Fig. 1. Pollutant molecules trapped within clay nanopores and interlayer spaces [31].

The research in this area has shown the value of clays in cleaning water. Studies on Albanian clays demonstrated their effectiveness in removing pesticides like metribuzin and methomyl [22, 23]. Further work confirmed that these natural and activated clays can significantly reduce concentrations of various pesticides and antibiotics in water [32], as illustrated in **Fig. 2**. The adsorption process typically follows well-known scientific models, with a rapid initial uptake of pollutants that slows down as the clay surfaces become full [27]. In swelling clays such as smectites (e.g., montmorillonite), the typical interlayer spacing (basal spacing) is about 1.0-1.5 nm when dry. When water or organic molecules enter the interlayer space, this distance can expand significantly, often reaching 1.8-2.0 nm for small polar organics and up to 2.5-3.5 nm or more when larger organic pollutants (e.g., phenols, pesticides, hydrocarbons) are intercalated. In practice, clays can accommodate a wide range of organic pollutants within these nanometer-scale interlayer galleries. There are several factors which influence the adsorption capacity of organic pollutants onto clays, mainly related to the properties of the clay, the pollutant, and the solution environment.

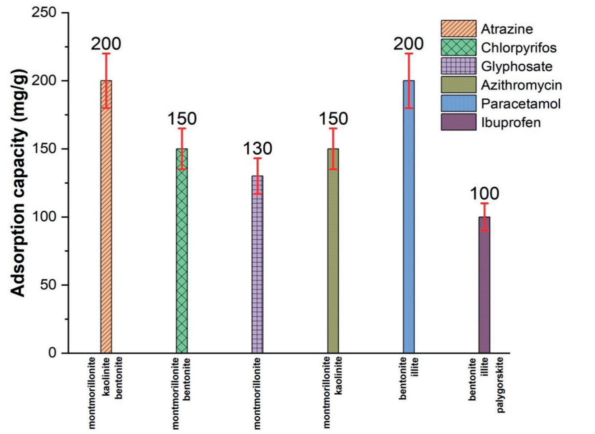

Fig. 2. Adsorption capacity versus clay type for different natural clays toward three pesticides and three pharmaceuticals.

Figure 2 shows the adsorption capacities of some natural clays toward three pesticides: Atrazine, Chlorpyrifos, Glyphosate and three pharmaceuticals mostly used during Covid 19 pandemic times, such as Azithromycin, Paracetamol, Ibuprofen. Natural clays such as montmorillonite, kaolinite, and bentonite have been reported to show adsorption capacities ranging up to 200 mg/g for atrazine, 150 mg/g for chlorpyrifos and approximately 130 mg/g for glyphosate [33, 34, 35, 36, 37]. Meanwhile, the adsorption capacities of azithromycin ranging up to 150 mg/g are reported for montmorillonite and kaolinite, 200 mg/g for paracetamol on bentonite, illite, and kaolinite and 100 mg/g for ibuprofen by bentonite, illite, and palygorskite [8, 9, 10,11,12].

Reviews of clay adsorption confirm its broad usefulness against a range of common pesticides [7]. A major advantage of clays is their global availability and low cost. They are found worldwide and can be processed inexpensively, making them ideal for large-scale water cleaning strategies [16, 22]. In order to increase the adsorbing capacities of natural clays, clay activation is performed. Clay activation refers to the physical, chemical, or thermal treatments applied to natural clays in order to improve their surface area, porosity, cation exchange capacity, and adsorption or catalytic properties. Since raw clays often have limited surface activity due to impurities, compact structure, or low reactivity, activation makes them more effective for applications in adsorption, catalysis, and environmental remediation. **Fig. 3** shows the influence of the adsorption capacity of three pesticides and three pharmaceuticals for the natural and activated clays. The increase of the adsorption capacities of all clays toward the selected organic pollutants with the clay activation has been observed. Activated clays have demonstrated maximal adsorption capacities exceeding 300 mg/g for atrazine and glyphosate; 200 mg/g for chlorpyrifos; 200 mg/g [38, 42] for azithromycin and ibuprofen and 300 mg/g for paracetamol [43, 44, 45, 46, 47. 48, 49]. These values are almost 50% higher compared to the adsorption capacities of the natural clays for the same analytes.

Modifying them with organic compounds can further enhance their selectivity and ability to capture specific pollutants like dyes [50, 51]. While clays are a powerful first step for removing organic pollutants, they are not sufficient on their own when the water is also contaminated with heavy metals. This is why they need to be combined with other materials, like manganese oxides, in composites.

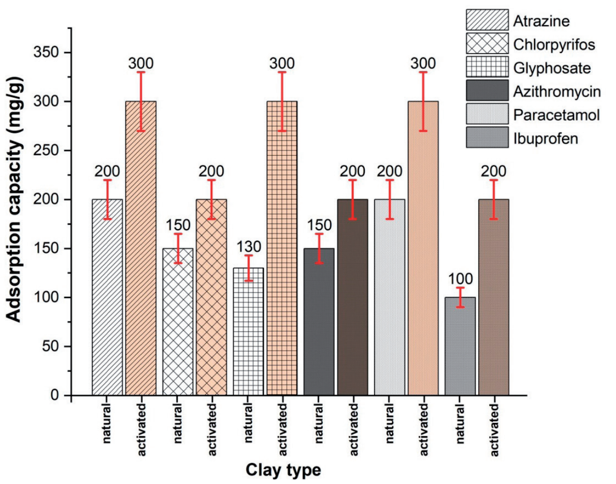

Fig. 3. The influence of the adsorption capacity of three pesticides and three pharmaceuticals for the natural and activated clays.

4. Birnessites, buserites, and heavy metal removal

While clays are excellent for organic pollutants, manganese oxides like birnessite (δ-MnO_2) and its hydrated form, buserite, are particularly effective for removing heavy metals [20, 19]. These minerals have a layered structure built from manganese-oxygen octahedra, with a high capacity for ion exchange and redox reactions [20, 18]. The layers in birnessite carry a negative charge, which is balanced by positively charged ions (e.g., Na^+, Ca^{2+}) and water molecules located between the layers [52]. The standard distance between these layers is about 7 Å. When water molecules enter this space, it expands to about 10 Å, transforming the material into buserite (**Fig. 4**). This hydration process is reversible and makes the material flexible, allowing it to accommodate large, hydrated metal ions [20].

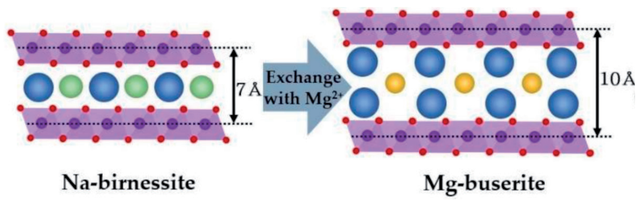

Fig. 4. Schematic structure of birnessite and buserite, showing the MnO_6 sheets, interlayer cations, and the expansion of the interlayer spacing upon hydration [53].

Heavy metals are captured through several mechanisms. These include ion exchange, where metal cations swap places with the ions in the interlayer space; surface complexation, where metals bind to oxygen atoms on the mineral surface; and sometimes redox reactions, where manganese changes oxidation state to trap the metal [19, 54]. Studies show that birnessite and buserite can effectively uptake toxic metals like lead, cadmium, copper, zinc, and mercury [21, 55, 56]. The hydration that creates buserite is especially important as it opens up the structure, improving the capture of these hydrated metal cations [20]. The adsorption capacity tends to be stronger for metals with larger hydrated ionic radii, such as lead and mercury, compared to smaller ones like cobalt [54] (**Fig. 5**).

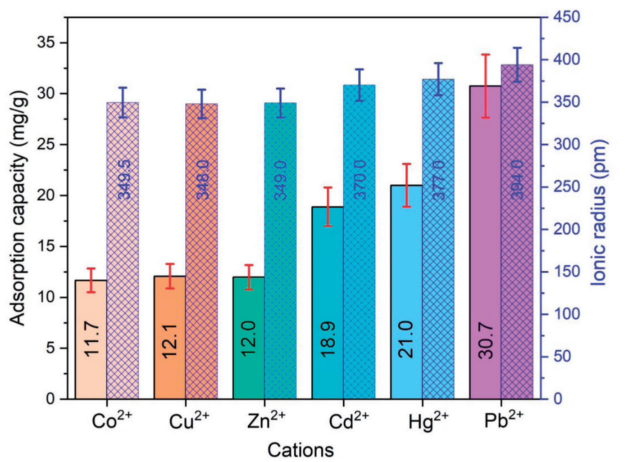

Fig. 5. Relationship between the adsorption capacity (left) of birnessites and the hydrated ionic radius (right) of various cations.

Early work on synthetic birnessites and buserites demonstrated their potential as remedies for environmental metal contamination [25]. Later research confirmed that the key to their effectiveness lies in the structural flexibility and mixed oxidation states of manganese, which control their selectivity and efficiency [57, 58]. This unique ability to change and adapt through hydration makes birnessites and buserites ideal partners for clays. Together, they can target the complex mixture of pollutants found in real-world water sources.

Regarding the ribbon graph of **Fig. 5** the adsorption capacity of Birnessites increases with the increase of the hydrated ionic radii. Thus Co^{2+} is less adsorbed compared to Cu^{2+}, Zn^{2+}, Cd^{2+}, Hg^{2+} and Pb^{2+}. This trend highlights the role of interlayer hydration and structural flexibility of Birnessites, where larger hydrated ions interact more strongly with the layered MnO_6 structure, leading to enhanced ion-exchange and adsorption efficiency.

5. Composite materials for universal water purification

In reality, polluted water rarely contains just one type of contaminant. It is often a complex mix of organic and inorganic substances. Combining clays and manganese oxides into a single composite material creates a multi-functional adsorbent that can handle this complexity [59]. In such a composite, the clays trap organic molecules through their interlayer spaces and surface interactions, while the manganese oxides remove toxic heavy metals through ion exchange and redox reactions [60, 61, 62]. The goal of this research is to propose a universal purification material, made of both, clays that birnessites/buserites as compact and efficient. Scientific models indicate that adsorption on these composites follows predictable patterns, with a fast initial removal rate that gradually slows as the material reaches its capacity [28, 27]. These composites can be manufactured into practical forms. For static applications, they can be shaped into spherical pellets or beads. This forms provide mechanical stability and a high surface area for contact [63]. This allows them to be used in fixed filters, packed columns, or simply dispersed directly into contaminated water bodies. For example, composites of montmorillonite clay and birnessite have been shown to simultaneously remove dyes and lead more effectively than either material alone [59]. Similarly, clay beads coated with manganese oxides have been used successfully in continuous-flow filter systems [30, 64].

The main advantage of these composites is their universality. A single material can target multiple classes of pollutants, simplifying the purification process and reducing the need for complex, multi-stage treatment plants. Their low cost, natural abundance and adaptability make them excellent candidates for a wide range of applications, from small household filters to large industrial wastewater treatment systems.

6. Static and dynamic remediation approaches

Two main approaches can be used to apply these composite materials for water purification: static and dynamic systems [65].

- In the static approach, the composite material is formed into spherical pellets or beads. These beads are then immersed directly into the polluted water body, where they remain stationary (**Fig. 6**).

Pollutants are removed through diffusion as the water moves around the beads. This spherical shape provides good mechanical stability, resistance to erosion, and a high surface area for contact with the water. The adsorption process follows a predictable pattern, with rapid initial clean-up that slows over time. This method is best suited for treating stagnant or slow-moving water, such as ponds, lakes, or reservoirs, though the clean-up speed can be limited by the rate of diffusion.

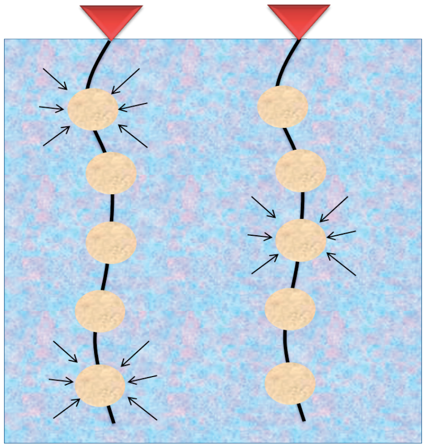

Fig. 6. Example of static composite spheres immersed in water, adsorbing pollutants.

- In the dynamic approach (**Fig. 7**), the composite material is packed into a filter system. Polluted water is pumped or flows through a compact bed of the material. The filter is often designed in layers.

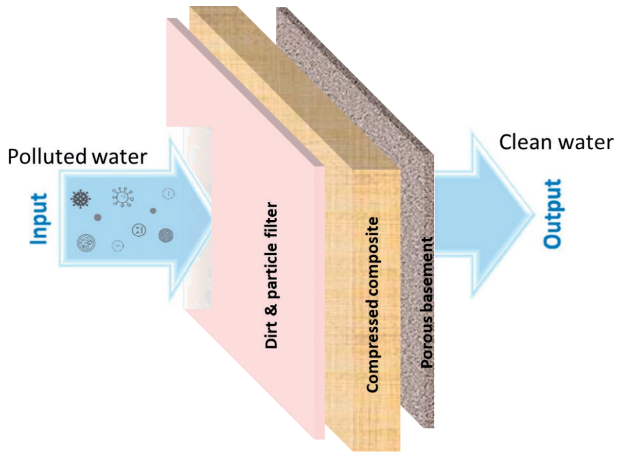

Fig. 7. Dynamic composite filter, showing a three-layer system with inflow of polluted water, a central composite layer for retention, and outflow of purified water.

A front layer might remove dirt and suspended particles, a central layer of the clay-manganese oxide composite adsorbs organic pollutants and heavy metals, and a final porous support layer ensures the filter remains stable and allows clean water to flow out steadily. This system is highly efficient for continuous-flow applications, like home water filters or industrial effluent treatment.

The main requirement is that the filter material must be replaced or regenerated once its adsorption sites are full.

7. Adsorbent management and sustainability

A critical aspect of any adsorption-based clean-up technology is managing the material after it has captured the pollutants. If not handled properly, used adsorbents can become a new source of contamination. For clay-birnessite composites, three main strategies are considered: (a) chemical regeneration and (b) thermal treatment [66], (c) integration with bioelectrochemical systems.

a) Chemical regeneration involves treating the saturated composite with specific aqueous solutions under controlled pH and temperature. Acidic or basic conditions can help to release (desorb) the organic pollutants and exchange the heavy metals back into the solution [65]. This process can restore some of the material's adsorption capacity, allowing it to be reused. However, it has drawbacks: it can be costly, and it generates a secondary stream of liquid waste that itself requires careful treatment to avoid causing further pollution [67]. Additionally, the regeneration process can slowly damage the structure of the adsorbent, reducing its efficiency over multiple cycles [66].

b) Thermal treatment offers a more straightforward and often more sustainable solution, especially at a large scale. In this method, the exhausted composites are heated to a high temperature (typically 400-600°C). This process, known as calcination, burns off and destroys the organic pollutants through combustion. The heavy metals remain within the resulting ash, where they are converted into stable oxides or other mineral phases. To prevent these metals from leaching out, the metal-laden ash is typically mixed into a cementitious matrix, creating concrete blocks that can be safely stored in controlled facilities or even used in construction [68]. This method safely immobilizes the pollutants for the long term. The energy required for heating is a significant operational cost. For a large-scale water treatment plant treating millions of liters per day, the thermal treatment of spent adsorbent could require a significant energy input. A preliminary estimate suggests that heating 1 ton of composite to 500°C could require approximately 150-200 kWh of energy. If powered by a dedicated renewable source, this would require, a small wind turbine (e.g., 10 kW capacity running at 30% capacity factor) to treat about 10-15 tons of spent material per month. While this is an additional cost, it avoids the creation of a secondary liquid waste stream and provides a permanently stabilized final product. The sustainability of this approach is maximized when the required heat is sourced from renewable energy, such as solar thermal or biogas, aligning with circular economy principles.

c) Integration with Bioelectrochemical Systems (BES), an innovative and sustainable approach to manage the secondary waste stream from chemical regeneration is to treat it using bioelectrochemical systems, such as microbial fuel cells (MFCs). The concentrated eluate from chemical regeneration, containing both desorbed organic pollutants and heavy metals, is often toxic and difficult to treat with conventional methods. BES offer a unique solution. In an MFC, electroactive bacteria oxidize the organic pollutants (e.g., pesticides, pharmaceuticals) at the anode, releasing electrons and protons. The heavy metals in the eluate can be simultaneously reduced and deposited at the cathode, achieving their removal and recovery [69, 70]. This integration is particularly synergistic with the materials discussed in this paper. Many advanced MFCs utilize clay-based separators and membranes due to their low cost, ion-exchange properties, and structural stability [71, 72]. Furthermore, manganese oxides have been explored as low-cost cathode catalysts to enhance oxygen reduction or direct metal reduction reactions [73]. Therefore, the very materials that form the core of our composite adsorbent (clays and birnessites) could be repurposed to build the BES reactor that treats its own waste stream. This creates a closed-loop or integrated system where the secondary pollution problem is solved by a technology built from the same abundant, low-cost materials, simultaneously recovering energy (as electricity) and valuable metals.

From a sustainability perspective, thermal immobilization provides long-term stability and avoids creating liquid waste streams. Its main drawback is the energy required for heating, which should ideally come from renewable sources to minimize the environmental footprint. Chemical regeneration is less energy-intensive but is more practical for small-scale or decentralized systems where the secondary waste can be managed locally. The choice between methods depends on the scale of the operation and the types of pollutants involved. Worth to mention here is that the sustainability of these composites is especially related to their abundance and the low cost. Clays are widely available and inexpensive [16, 22], and manganese oxides can be synthesized from common precursors. This makes the composite technology an accessible and scalable solution, particularly valuable for regions that lack advanced water treatment infrastructure. Recent research has shown that local clays can be successfully shaped into pellets for pesticide removal, demonstrating the strong potential for integrating them into these kinds of composite systems [7, 17, 22, 23]. The availability of both static and dynamic methods makes these composites highly adaptable to different environmental needs and scales of operation.

8. Cost considerations for deployment

The proposed clay-birnessite composite offers several inherent cost advantages. The raw materials, natural clays and manganese precursors are abundant and inexpensive. Clay minerals are globally available and can often be sourced locally, significantly reducing transportation costs. Manganese is also a common element, and birnessites can be synthesized using relatively simple and low-energy wet chemistry methods [20, 25]. The manufacturing of the composite into pellets or beads, while adding a processing step, utilizes standard equipment from the ceramics and materials industry, keeping production costs moderate. When comparing the cost to conventional adsorbents like granular activated carbon (GAC), which can cost 1,500-2,500 USD/ton, the clay-based composite is projected to be significantly cheaper, potentially in the range of 300-500 USD/ton, together with an estimation of potential water treatment capacity per ton of adsorbent. This is calculated considering the following approximations: natural clays ~30-100 USD/ton, acid-activated clays ~150-300 USD/ton, and synthetic birnessite ~400-800 USD/ton at laboratory scale. Since GAC is primarily effective for organic compounds and requires thermal regeneration, the clay-birnessite composite targets both organics and inorganics. Its potential for low-cost chemical regeneration or its ability to be thermally treated and safely immobilized without the need for complex reactivation processes can offer long-term operational savings. The integration with BES for waste stream treatment, while requiring initial capital investment, offers the potential for energy recovery and metal recuperation, offsetting operational costs over the system's lifetime. A detailed life-cycle cost analysis, including raw material extraction, manufacturing, transportation, operation, and end-of-life management, would be the next step to fully quantify the economic benefits and optimize the design for specific applications.

9. Conclusions

This study sheds light on the strong potential of clay minerals, layered manganese oxides, and their composites as effective, low-cost materials for water remediation in the context of increasing global water pollution and scarcity. The synthesis of experimental evidence from previous work and an extensive review of the literature clearly demonstrates that natural clays, particularly montmorillonite, kaolinite, bentonite, illite, and palygorskite, are highly efficient adsorbents for a wide range of organic pollutants. Selected pesticides such as atrazine, chlorpyrifos, and glyphosate, as well as pharmaceutical contaminants including azithromycin, paracetamol, and ibuprofen, show substantial adsorption onto clay surfaces and interlayer spaces. Natural clays already exhibit significant uptake capacities, while activated and chemically modified clays display markedly enhanced adsorption, often reaching or exceeding 200-300 mg/g, confirming the crucial role of surface modification and interlayer chemistry in optimizing performance. In parallel, the study underlines the exceptional capacity of layered manganese oxides, such as birnessites and their hydrated form, buserites for the removal of toxic heavy metal cations from water. These materials efficiently capture metals such as Pb^{2+}, Cd^{2+}, Cu^{2+}, Zn^{2+}, and Hg^{2+} through ion exchange, surface complexation, and redox-driven mechanisms. Natural birnessites and buserites show adsorption capacities up to about 400 mg/g, while synthetic and sodium-exchanged variants can exceed 600 mg/g, with adsorption strength closely linked to interlayer hydration and the hydrated ionic radius of the metal cations.

The main conclusion of this study is that combining clays and birnessites/buserites into a single composite material represents a highly promising strategy for universal water purification. Such composites can simultaneously target organic pollutants and heavy metals, reflecting the complex mixtures typically present in real contaminated waters. Conceptual designs involving compact spherical pellets or filter-packed systems offer practical routes for both static and dynamic remediation applications.

Importantly, the abundance, low cost, and environmental compatibility of clays and manganese oxides make these composites particularly suitable for large-scale deployment, including in regions with limited access to advanced water treatment technologies. The long-term sustainability of this technology depends not just on adsorption performance, but also on the responsible management of the employed material. Both chemical regeneration and thermal immobilization offer viable pathways to ensure that the composites do not become secondary pollutants. Thermal treatment, in particular, which incorporates the metal-laden residue into concrete, aligns well with circular economy principles by creating a stable, safe end product. Furthermore, the innovative integration of chemical regeneration with bioelectrochemical systems presents a forward-thinking solution to manage secondary waste streams, potentially recovering energy and metals while utilizing the same family of low-cost clay and manganese materials. A preliminary cost analysis suggests the composite is economically competitive with conventional adsorbents, reinforcing its potential for widespread adoption. A follow up of this study should focus on pilot-scale testing of these composites in dynamic flow systems, optimizing the composite ratio for specific pollutant mixtures, and conducting a full life-cycle assessment to validate the sustainability and economic benefits outlined here.

10. References

[1] Crini, G., & Lichtfouse, E. (2019). Advantages and disadvantages of techniques used for wastewater treatment. *Environmental Chemistry Letters*, 17, 145–155.

[2] World Health Organization. (2022). Drinking-water Fact Sheet. Retrieved from https://www.who.int/news-room/fact-sheets/detail/drinking-water.

[3] Delle Site, A. (2001). Factors affecting sorption of organic compounds in natural sorbent/water systems and sorption coefficients for selected pollutants. A review. *Journal of Physical and Chemical Reference Data*, 30(1), 187–439.

[4] Zango, Z. U., Garba, A., Garba, Z. N., Usman, F., & Lim, J.-W. (2022). Montmorillonite for adsorption and catalytic elimination of pollutants from wastewater: A state-of-the-art review. *Sustainability*, 14(24), 16441.

[5] Lagaly, G. (2001). Pesticide–clay interactions and formulations. *Applied Clay Science*, 18(5-6), 205–209.

[6] Karapanagioti, H. K., Kleineidam, S., Sabatini, D. A., Grathwohl, P., & Ligouis, B. (2006). Adsorption of pesticides on kaolinite and montmorillonite as a function of hydrophobicity. *Environmental Science & Technology*, 40(7), 2357–2362.

[7] Isak, N., & Xhaxhiu, K. (2023). A review on the adsorption of diuron, carbaryl, and alachlor using natural and activated clays. *Remediation Journal*, 33(4), 339–353.

[8] Cela-Dablanca, R., Barreiro, A., Rodríguez-López, L., Pérez-Rodríguez, P., Arias-Estévez, M., Fernández-Sanjurjo, M. J., Álvarez-Rodríguez, E., & Núñez-Delgado, A. (2022). Azithromycin Adsorption onto Different Soils. *Processes*, 10, 2565.

[9] Hacıosmanoğlu, G. G., Mejías, C., Martín, J., Santos, J. L., Aparicio, I., & Alonso, E. (2022). Antibiotic adsorption by natural and modified clay minerals as designer adsorbents for wastewater treatment: A comprehensive review. *Journal of Environmental Management*, 317, 115397.

[10] Aydin, S., Celik Karakaya, M., Karakaya, N., & Aydin, M. E. (2023). Effective removal of selected pharmaceuticals from sewerage treatment plant effluent using natural clay (Na-montmorillonite). *Applied Water Science*, 13(6), 129.

[11] Mansouri, F., Chouchene, K., Wali, A., Labille, J., Roche, N., & Ksibi, M. (2024). Adsorption of anti-inflammatory and analgesic drugs traces in water on clay minerals. *Chemosphere*, 353, 141469.

[12] H. Khazri, I. Ghorbel-Abid, R. Kalfat, and M. Trabelsi-Ayadi, "Removal of ibuprofen, naproxen and carbamazepine in aqueous solution onto natural clay: Equilibrium, kinetics, and thermodynamic study," *Applied Water Science*, vol. 6, no. 2, pp. 147–159, 2016.

[13] Ali, I., Alharbi, O. M. L., & Alothman, Z. A. (2021). Advances in wastewater treatment technologies: An overview. In: *Water Pollution and Management Practices. Singapore: Springer*, pp. 1-22.

[14] Zhang, Y., Wu, B., Xu, H., Liu, H., Wang, M., He, Y., & Pan, B. (2019). Nanomaterials-enabled water and wastewater treatment. *NanoImpact*, 3, 22–39.

[15] Crini, G., Lichtfouse, E., Wilson, L. D., & Morin-Crini, N. (2019). Adsorption-oriented processes using conventional and non-conventional adsorbents for wastewater treatment. In: *Green Adsorbents for Pollutant Removal. Cham: Springer*, pp. 23–71.

[16] Murray, H. H. (2000). Traditional and new applications for kaolin, smectite, and palygorskite: a general overview. *Applied Clay Science*, 17(5-6), 207–221.

[17] Isak, N., Xhaxhiu, K., Behrami, E., & Andoni, A. (2023). A comparative study of the adsorption and desorption process of selected natural Albanian clays toward methomyl and dimethoate pesticides. *Journal of Environmental Management*, 346, 118989.

[18] Post, J. E. (1999). Manganese oxide minerals: Crystal structures and economic and environmental significance. *Proceedings of the National Academy of Sciences*, 96(7), 3447–3454.

[19] Liu, P., Ptacek, C. J., & Blowes, D. W. (2018). Removal of arsenic and heavy metals by natural and synthetic manganese oxides. *Water Research*, 133, 50–60.

[20] Feng, X., Kanoh, H., & Ooi, K. (2010). Manganese oxide porous crystals. *Journal of Materials Chemistry*, 9(12), 319–333.

[21] Villalobos, M., Bargar, J., & Sposito, G. (2005). Mechanisms of Pb(II) sorption on a biogenic manganese oxide. *Environmental Science & Technology*, 39(2), 569–576.

[22] Xhaxhiu, K., Shllaku, J., Sula, L., Xhelaj, A., & Kota, T. (2013a). The removal of metribuzin from pesticide contaminated waters using natural- and activated Prrenjasi clay. *Natura Montenegrina*, 12(2), 505–519.

[23] Xhaxhiu, K., Sula, L., Shllaku, J., Xhelaj, A., & Kota, T. (2013b). Comparison of the adsorption capacities of two Albanian clays for the removal of metribuzin. *Natura Montenegrina*, 12(3-4), 949–965.

[24] Xhaxhiu, K., Prifti, E., & Zitka, O. (2020). A case study of methomyl removal from aqueous solutions by four natural Albanian clays. *Remediation Journal*, 30(3), 89–100.

[25] Xhaxhiu, K. (2015). Synthetic Birnessites and Buserites as heavy metal cation traps and environmental remedies. *Journal of Metallomics and Nanotechnologies*, II(3), 23–32.

[26] Önal, M., Sarıkaya, Y., Alemdaroğlu, T., & Bozdogan, I. (2007). The effect of acid activation on some physicochemical properties of a bentonite. Turkish *Journal of Chemistry*, 31(4), 435–442.

[27] Langmuir, I. (1918). The adsorption of gases on plane surfaces of glass, mica and platinum. Journal of the *American Chemical Society*, 40(9), 1361–1403.

[28] Freundlich, H. M. F. (1906). Over the adsorption in solution. *Zeitschrift für Physikalische Chemie*, 57(A), 385–470.

[29] Sposito, G. (1984). The Surface Chemistry of Soils. New York: Oxford University Press.

[30] Babatunde, A. O., & Zhao, Y. Q. (2010). Constructive approaches to the use of natural and modified clays for pollutant removal. *Critical Reviews in Environmental Science and Technology*, 40(9), 791–821.

[31] Cornell Chronicle. (2016). Study: Antibiotics hide within soil mineral layers. Retrieved from https://news.cornell.edu/stories/2016/02/study-antibiotics-hide-within-soil-mineral-layers.

[32] Prifti, E., Isak, N., & Xhaxhiu, K. (2021). Study of desorption of some insecticides from four natural Albanian clays. *International Journal of Ecosystems and Ecology Science*, 11(3), 415–426.

[33] Fruhstorfer, P., Schneider, R. J., Weil, L., & Niessner, R. (1993). Factors influencing the adsorption of atrazine on montmorillonitic and kaolinitic clays. *Science of the Total Environment*, 138(1–3), 317–328.

[34] Salomón, Y. L., Georgin, J., Allasia, D. G. P., Netto, M. S., Aniagor, C. O., Ighalo, J. O., & Franco, D. S. P. (2025). A Comprehensive Review on Atrazine Adsorption: From Environmental Contamination to Efficient Removal Technologies. *Sustainability*, 17(23), 10455.

[35] de Santana, H., Toni, L. R. M., Benetoli, L. O. de B., Zaia, C. T. B. V., Rosa, M., & Zaia, D. A. M. (2006). Effect in glyphosate adsorption on clays and soils heated and characterization by FT–IR spectroscopy. *Geoderma*, 136(3–4), 738–750.

[36] Besghaier, S., Cecilia, J. A., Chouikhi, N. et al. (2022). Glyphosate adsorption onto porous clay heterostructure (PCH): kinetic and thermodynamic studies. *Brazilian Journal of Chemical Engineering*, 39, 903–917.

[37] Masini, J. C., & Abate, G. (2021). Guidelines to Study the Adsorption of Pesticides onto Clay Minerals Aiming at a Straightforward Evaluation of Their Removal Performance. *Minerals*, 11(11), 1282.

[38] Ajala, O. J., Nwosu, F. O., & Ahmed, R. K. (2018). Adsorption of atrazine from aqueous solution using unmodified and modified bentonite clays. *Applied Water Science*, 8, 214.

[39] Liu, H., Chen, W., Liu, C., Liu, Y., & Dong, C. (2014). Magnetic mesoporous clay adsorbent: Preparation, characterization and adsorption capacity for atrazine. *Microporous and Mesoporous Materials*, 194, 72–78.

[40] Suciu, N. A., & Capri, E. (2009). Adsorption of chlorpyrifos, penconazole and metalaxyl from aqueous solution by modified clays. *Journal of Environmental Science and Health, Part B*, 44(6), 525-532.

[41] Qurie, M., Khamis, M., Ayyad, I., Scrano, L., Lelario, F., Bufo, S. A., Mecca, G., & Karaman, R. (2016). Removal of chlorpyrifos using micelle–clay complex and advanced treatment technology. *Desalination and Water Treatment*, 57(33), 15687–15696.

[42] Damonte, M., Torres Sánchez, R. M., & dos Santos Afonso, M. (2007). Some aspects of the glyphosate adsorption on montmorillonite and its calcined form. *Applied Clay Science*, 36(1–3), 86–94.

[43] Diab, A. S., Rudayni, H. A., Mohamed, R. A. et al. (2025). Green clay engineering via dimethyl sulfoxide, dimethylformamide, and urea-assisted exfoliation of

serpentinite for efficient azithromycin adsorption as emerging pharmaceutical pollutant. *Scientific Reports*, 15, 35279.

[44] Imanipoor, J., Mohammadi, M., & Dinari, M. (2021). Evaluating the performance of L-methionine modified montmorillonite K10 and 3-aminopropyltriethoxysilane functionalized magnesium phyllosilicate organoclays for adsorptive removal of azithromycin from water. *Separation and Purification Technology*, 275, 119256.

[45] Shekhawat, H., Kumari, A., Raol, H., & Choudhury, T. (2024). Preparation and characterization of clay hybrid adsorbents for the removal of paracetamol from model wastewater: A comparative study. *Applied Clay Science*, 258, 107469.

[46] Allaoui, I., El Mourabit, M., Arfoy, B., Hadri, M., Barhoun, A., & Draoui, K. (2024). Adsorption equilibrium, kinetic, and thermodynamic studies on the removal of paracetamol from wastewater using natural and HDTMA-modified clay. *Desalination and Water Treatment*, 318.

[47] Elamin, M. R., Abdulkhair, B. Y., Algethami, F. K. et al. (2021). Linear and nonlinear investigations for the adsorption of paracetamol and metformin from water on acid-treated clay. *Scientific Reports*, 11, 13606.

[48] Malvar, J. L., Martín, J., del Mar Orta, M., Medina-Carrasco, S., Santos, J. L., Aparicio, I., & Alonso, E. (2020). Simultaneous and individual adsorption of ibuprofen metabolites by a modified montmorillonite. *Applied Clay Science*, 189, 105529.

[49] Choi, J., & Shin, W. S. (2020). Removal of Salicylic and Ibuprofen by Hexadecyltrimethylammonium-Modified Montmorillonite and Zeolite. *Minerals*, 10(10), 898.

[50] Kloprogge, J. T., Komarneni, S., & Amonette, J. E. (1999). Synthesis of smectite clay minerals: a critical review. *Clays and Clay Minerals*, 47(5), 529–554.

[51] Alver, E., & Metin, A. Ü. (2012). Anionic dye removal from aqueous solutions using modified zeolite: Adsorption kinetics and isotherm studies. *Chemical Engineering Journal*, 200-202, 59–67.

[52] McKenzie, R. M. (1989). Manganese oxides and hydroxides. In: Dixon, J. B. & Weed, S. B. (Eds.) Minerals in Soil Environments (2nd ed.). SSSA Book Series, pp. 439–465.

[53] Min, S., & Kim, Y. (2020). Physicochemical Characteristics of the Birnessite and Todorokite Synthesized Using Various Methods. *Minerals*, 10(10), 884.

[54] Manceau, A., & Charlet, L. (1992). X-ray absorption spectroscopic study of the sorption of Cr(III) at the oxide-water interface. *Journal of Colloid and Interface Science*, 148(2), 425–442.

[55] Toner, B., Manceau, A., Marcus, M. A., Millet, D. B., & Sposito, G. (2006). Zinc sorption by a bacterial biofilm: X-ray absorption fine-structure spectroscopy and protein fluorescence studies. *Environmental Science & Technology*, 40(20), 6523–6529.

[56] Grangeon, S., Lanson, B., & Lanson, M. (2014). Solid-state transformation of nanocrystalline phyllomanganate into tectomanganate: influence of initial layer spacing. *American Mineralogist*, 99(7), 1345–1354.

[57] Simanova, A. A., & Persson, P. (2010). Characterization of gallium (III) adsorption on hydrous manganese oxide. *Environmental Science & Technology*, 44(3), 1045–1051.

[58] Yu, Q., Sasaki, K., Tanaka, K., & Ohnuki, T. (2013). Structural factors of biogenic birnessite produced by fungus Paraconiothyrium sp. WL-2 strain affecting sorption of Co^{2+}. *Geochimica et Cosmochimica Acta*, 113, 1–16.

[59] Jiang, Y., & Zhang, Y. (2019). Montmorillonite–birnessite composite for simultaneous removal of methylene blue and Pb(II). *Clay Minerals*, 54(3), 299–306.

[60] Peña, J., Bargar, J. R., & Sposito, G. (2015). Copper sorption by the edge surfaces of synthetic birnessite nanoparticles. *Chemical Geology*, 397, 24–32.

[61] Wang, Y., Feng, X., Villalobos, M., Tan, W., & Liu, F. (2012). Sorption behavior of heavy metals on birnessite: Relationship with its Mn average oxidation state and implications for types of sorption sites. *Chemical Geology*, 292-293, 25–34.

[62] Yu, Q., Sasaki, K., & Hirajima, T. (2016). Synthesis of todorokite at atmospheric pressure for efficient removal of Pb^{2+} and Cd^{2+} from wastewater. *Journal of Hazardous Materials*, 301, 332–340.

[63] Mohan, D., & Pittman, C. U. (2007). Arsenic removal from water/wastewater using adsorbents - A critical review. *Journal of Hazardous Materials*, 142(1-2), 1–53.

[64] Ali, I., Asim, M., & Khan, T. A. (2012). Low cost adsorbents for the removal of organic pollutants from wastewater. *Journal of Environmental Management*, 113, 170–183.

[65] Srivastava, V. C., Mall, I. D., & Mishra, I. M. (2008). Equilibrium modeling of ternary adsorption of metal ions onto rice husk ash. *Journal of Chemical & Engineering Data*, 54(3), 705–711.

[66] Suresh, S., Srivastava, V. C., & Mishra, I. M. (2012). Adsorption of catechol, resorcinol, hydroquinone, and their derivatives: a review. *International Journal of Energy and Environmental Engineering*, 3(1), 1–19.

[67] Nethaji, S., Sivasamy, A., & Mandal, A. B. (2013). Preparation and characterization of corn cob activated carbon coated with nano-sized magnetite particles for the removal of Cr(VI). *Bioresource Technology*, 134, 94–100.

[68] Zhang, W., & Qian, L. (2019). Immobilization of cadmium and lead in contaminated soil using amendments: a review. *Pedosphere*, 29(3), 265–276.

[69] Nancharaiah, Y. V., Venkata Mohan, S., & Lens, P. N. L. (2015). Metals removal and recovery in bioelectrochemical systems: A review. Bioresource Technology, 195, 102-114.

[70] Wang, H., & Ren, Z. J. (2014). A comprehensive review of microbial electrochemical systems as a platform technology. Biotechnology Advances, 31(8), 1796-1807.

[71] Gajda, I., Greenman, J., & Ieropoulos, I. A. (2018). Recent advancements in real-world microbial fuel cell applications. Current Opinion in Electrochemistry, 11, 78-83.

[72] Behera, M., & Ghangrekar, M. M. (2017). Performance of microbial fuel cell using clayware as separator. Journal of Hazardous Materials, 190(1-3), 112-117.

[73] Zhang, L., Liu, C., Zhuang, L., Li, W., Zhou, S., & Zhang, J. (2019). Manganese dioxide as an alternative cathodic catalyst to platinum in microbial fuel cells. Biosensors and Bioelectronics, 24(9), 2825-2829.

Engineering Power – *Bulletin of the Croatian Academy of Engineering*

Vol. 21(1) 2026 – ISSN 2718-322X (Online)

Publisher: Croatian Academy of Engineering (HATZ), 28 Kačić Street, P.O. Box 14, HR-10000 Zagreb, Republic of Croatia

Editor-in-Chief: Prof. Vedran Mornar, Ph.D., President of the Academy
University of Zagreb Faculty of Electrical Engineering and Computing

Editor: Prof. Bruno Zelić, Ph.D., Vice-President of the Academy
University of Zagreb Faculty of Chemical Engineering and Technology

Guest Editor: Prof. Neven Duić, Ph.D., University of Zagreb, Faculty of Mechanical Engineering and Naval Architecture

Activities Editor: Tanja Miškić Rogić

Editorial Board Address: Croatian Academy of Engineering (HATZ), "Engineering Power" – Bulletin of the Croatian Academy of Engineering, Editorial Board, 28 Kačić Street, P.O. Box 14, HR-10000 Zagreb, Republic of Croatia

E-mail: hatz@hatz.hr

Graphical and Technical Editor: Tiskara Zelina, Ltd., Zelina

The publication of the Engineering Power journal was financially supported by the Ministry of Science, Education and Youth within the project Strengthening publishing activities, cooperation with industry, and the national and international visibility of technical and biotechnical sciences through the programmes and activities of the Croatian Academy of Engineering, pursuant to the Financial Assistance Agreement dated May 20, 2026.